THE UNIVERSITY OF TEXAS AT AUSTIN

# A Theoretical Investigation of Supernovae Progenitors

Sarafina Nance

May 2, 2016

## 1 INTRODUCTION

Core-collapse supernovae (CCSN) play a pivotal role in astronomy by providing unique laboratories to explore the laws of basic physics. The four known forces of nature–gravity, electromagnetism, and the strong/weak nuclear force–all drive supernovae processes on various length and time scales (**?**). Thus, supernovae (SN) offer unique settings to study strange and exotic phenomena in the universe. Supernovae represent the explosive stellar deaths of massive and ancient stars, forming a variety of core processes in the universe. These cataclysmic explosions are some of the most energetic events in the universe, releasing $10^{51}$ ergs of luminosity (on the order of 100 million suns) into their surrounding environments. They therefore create the unique conditions for nucleosynthesis, permanently altering the interstellar medium and generating cosmic rays. Supernovae also are the birth sites for neutron stars and black holes, two of the most exotic features of our universe. Finally, they act as cosmological distance markers. This final revelation heralded the discovery of dark energy– one of the most important discoveries of modern science.

In an effort to give a general overview of supernova dynamics, we summarize the explosion process here. Massive stars greater than $M \gtrsim 8M_{\odot}$ develop shell burning over their lifetimes, simultaneously growing the central core while fusing progressively heavier and heavier elements (**?**). Ultimately, the core is destabilized when iron dissolves into its constituent particles– alpha, protons, and neutrons– that absorb energy and destabilize the core. The inner core thencollapses and rebounds into the surrounding shells (**?**). This collapse generates a shock front that expands into the surrounding medium, slamming into previously expelled material from the stellar envelope.

Due to the complex dynamics of the gravitational collapse and ensuing explosion, supernovae are difficult to study theoretically (**?**). However, it is possible to create 1-D (and, more recently, 3-D) simulations of the explosive event. In the following two studies, we take a two-part theoretical approach to investigating supernovae by using `MESA` stellar evolution code. In Study I, we propose a general framework to understanding supernovae and their progenitors by investigating the basic demarcation between type I (hydrogen-poor) and type II (hydrogen-rich) SN. Detecting trace hydrogen in post-explosion spectra lead to deeper understanding of the evolution of the progenitor systems. We calculate `MESA` models to determine which zero-age main sequence (ZAMS) masses retain trace amounts of hydrogen just prior to explosion.

To better understand SN progenitors, we then perform a case study (Study II) of Betelgeuse, a massive red supergiant in the constellation Orion, to determine when it will explode as a supernova. We once again use `MESA` to compute a series of rotating and non-rotating models over a 10 $M_\odot$ range, in 1 $M_\odot$ intervals. Because Betelgeuse has a large extended envelope, the inner core cannot be seen. As a result, we take an asteroseismological approach by computing characteristic frequencies of convective zones constrained by the evolutionary state set by observed values of R, $T_{eff}$, L, and rotation velocity.

In the following sections, we introduce Studies I & II to develop a theoretical study of supernovae progenitors.

## REFERENCES

A. M. G. M.-P. B. M. H.-Th. Jankaa, K. Langankeb. Theory of core-collapse supernovae. *Physics Reports*, 442:38–74, 2007.

L. H. A. M.-B. M. Hans-Thomas Janka, Florian Hanke and M. Obergaulinger. Core-collapse supernovae: Reflections and directions. *Progress of Theoretical and Experimental Physics*, (1A309), 2013.

Draft version August 7, 2015
Preprint typeset using LaTeX style emulateapj v. 12/16/11

# FINGERPRINTING HYDROGEN IN CORE-COLLAPSE SUPERNOVAE

S. Nance[1], J. Parrent[2], A. Soderberg[2], et al.

*Draft version August 7, 2015*

## ABSTRACT

This is a preliminary report on the mass of remaining hydrogen envelopes for stars massive enough to explode under core collapse. Using the stellar evolution code, MESA, our initial findings suggest that a significant fraction of massive stars with $M_{ZAMS} = 20 - 60 M_\odot$ lose all but $10^{-3} M_\odot - 10^{-1} M_\odot$ as they near eventual core collapse. This result is dependent on the mass-loss prescription, degree of rotation, metallicity, rates of nuclear burning in the core, and the final stellar configuration. Nevertheless, each of our test cases include a few stars that retain trace amounts of surface hydrogen, which would then be detected as faint H$\alpha$ in type IIb/Ib/Ic supernova spectra. We also compare our findings to the progenitor candidate identified for iPTF13bvn using the most recent photometric corrections, and we confirm a previous conclusion found by Groh et al. (2013) that the progenitor had an initial mass of $32 M_\odot$, but now with an additional condition of $0.06 M_\odot$ of hydrogen on its surface just prior to the explosion.

*Keywords:* supernovae: general — stars: evolution — binaries: general — stars: massive — stars: Wolf-Rayet

## 1. INTRODUCTION

When stars with a zero-age main sequence (ZAMS) mass $M \gtrsim 8 M_\odot$ extinguish an inner reservoir of fuel, a core-collapse event ensues, where the iron core collapses into either a neutron star or black hole. The collapse generates a shockwave that ejects several solar masses of irradiated material, along with any remaining hydrogen-rich envelope, into the surrounding medium. Prior to the explosion, these stars tend to lose some fraction of their hydrogen-rich envelope via winds or interaction with a companion as they evolve beyond the main-sequence of core-hydrogen burning (Glebbeek et al. 2009).

High cadence spectroscopic monitoring of the ensuing supernova (SN) can provide important clues about the identity and final state of the original system. Yet to be resolved, however, is how evolutionary models of massive stars correspond to the observed zoo of explosive stellar endpoints. Thus, in order to use stellar models as theoretical constraints for SN progenitors, we must check that they can also emulate well observable spectroscopic constraints.

SN are generally classified into two regimes: hydrogen poor type I, and hydrogen rich type II (see Figure 1). SN Ia are unique in that they result from the death of evolved white dwarf progenitors (Nugent et al. 2011). Other types of SN, however, are thought to result from some form of a core-collapse supernovae (CCSN). Thus, the majority of CCSN observed are believed to follow a well-determined spectral sequence in terms of the strength of H$\alpha$ (Minkowski 1941; Filippenko 1997). While the strength and presence of hydrogen further demarcates the classes of SN Ib/c and SN II, faint signatures of H$\alpha$ are likely detectable for some, if not all, type I CCSN (Wheeler et al. 1995; Parrent et al. 2015; and see Figure 1). However, spectrum synthesis calculations have yet to estimate the corresponding mass of remaining hydrogen (Filippenko 1997), much less determine why the top layer of hydrogen-rich ejecta is more extended for such broad-lined events. From greatest to least mass, the hydrogen envelope mass sequence seems to follow the spectral sequence, IIP/L $\rightarrow$ IIb $\rightarrow$ Ib $\rightarrow$ Ic. (For a summary of this relation, see Table 1.)

SN II can be divided into the sub-classes: IIP, IIL, IIn, and IIb, where the P Cygni profile in H$\alpha$ acts as relatively reliable indicator of unburned hydrogen in the fast-moving ejecta ($\sim 10^3$ km s$^{-1}$) (see Parrent et al. 2015). SN IIL and SN IIP are characterized by linear and plateau declines, respectively, in their bolometric light curves (Sanders et al. 2014). Thus, it would make sense for SN II to result from the explosion of a star during its red or yellow supergiant phase of evolution. SN IIb tend to retain the weak H$\alpha$ hallmark of SN II, but later assume time-dependent signatures of He I resembling SN Ib (Filippenko 1988). For these SN, the mass of the progenitor's extended envelope is thought to be on the order of $10^{-2}$–$10^{-1}$ $M_\odot$ (Smith 2015). By contrast, this is significantly less than the $\sim 5$ $M_\odot$ of hydrogen estimated in the ejecta of some SN II (Smartt 2015). This seems to further suggest that intermittent periods of mass loss may be the root cause of spectroscopic diversity among hydrogen-rich and hydrogen-poor supernovae (see Smith 2015; Smartt 2015; Yoon 2015 for reviews). SN IIn, on the other hand, contain strong narrow emission of H$\alpha$ and H$\beta$, thereby indicating the ejecta have either photoionized or physically interacted with progenitor material that was lost prior to the explosion (see Taddia et al. 2012).

SN I, on other hand, possess much weaker 6250 Å signatures than those of type II, and are therefore well-placed for interpretation as faint H$\alpha$. If true, this would imply SN Ib/Ic spectra harbor faint signatures of H$\alpha$ (and helium) that are consistent with $\sim 10^{-3} M_\odot - 10^{-1} M_\odot$ of depleted hydrogen-rich material (see James & Baron 2010). Conspicuous signatures near

[1] Department of Astronomy, University of Texas, Austin, TX 78712, USA
[2] Harvard-Smithsonian Center for Astrophysics, 60 Garden St., Cambridge, MA 02138, USA

6250 Å in the spectra of a number of super-luminous supernovae, in addition to some gamma-ray bursts (GRBs) and faint, fast-evolving SN Ib/c, could also be H$\alpha$. Post-explosion spectra of supernovae, however, do not yet provide strong mass constraints on the remaining mass of hydrogen in the ejecta of CCSN (Parrent et al. 2015).

Meanwhile, progenitor systems of SN Ib/c remain highly debated (Matheson et al. 2001). Some studies suggest evolved Wolf-Rayet (WR) stars as progenitors (Groh et al. 2013), while others name variable mass-stripping due to close interaction with a companion (Yoon 2015). Because the canonical 6250 Å spectral feature in SN Ib/c spectra is likely dominated by faint H$\alpha$ (see Parrent et al. 2015), which contradicts the assumption of SN Ib/c as hydrogen-free, it remains to be seen whether detections of small amounts of unburned hydrogen impacts candidate progenitor systems.

Here we investigate evolutionary models of stars using the 1D Modules for Stellar Experiments in Astrophysics code (`MESA` version 7624; Paxton et al. 2015) in an effort to predict the range of ZAMS masses that retain a layer of $10^{-3}$, $10^{-2}$, $10^{-1}$, and $1-5$ $M_\odot$ of hydrogen just prior to the supernova event. In § 2 we outline our methods and basic input parameters for a few mass ranges of single and binary systems. In § 3 we present our results. In § 4 we summarize our findings and address a few implications for trace amounts of unburned hydrogen envelopes. In § 5, we highlight a few unanswered questions and look toward additional test cases for resolve.

## 2. METHODS

We use theoretical `MESA` models to trace the evolution of a given star from ZAMS to near core-collapse. `MESA` produces temperature-density (TRho) (see Figure 6 for an example), abundance, and Kippenhahn profiles (amongst others) to visualize a star's evolutionary progress.

In this work, we focus on the abundance plots near core-collapse to document hydrogen masses that are greater than or equal to estimates obtained from post-explosion spectrum synthesis calculations resembling SN Ib/Ic/IIb. In this sense, the abundance profiles are essential to collecting accurate predictions for progenitor types and evolutionary tracks.

Initial modeling with `MESA` reveals little change between the onset of core Si-burning and the final stage just before the core collapse; observables such as surface luminosity and temperature differ by $\sim 5\%$. We therefore halt the calculation when the core silicon abundance reaches 10% of total abundance to save time and explore a larger initial mass range. In a forthcoming work, we will evolve the stars until the run is terminated.

### 2.1. *Model Parameters*

To facilitate our investigation, we call upon files called "`inlist`s" in `MESA`. An `inlist` file holds variable parameters for specific runs. We included one set of `inlist`s for our single star systems, and another set for the binary star systems.

In the case of isolated stars, our primary free parameter of interest is the initial ZAMS mass. We choose masses that likely represent Wolf-Rayet (WR) stars ($\sim 10-80 M_\odot$; see Crowther 2007 for a review). For the non-rotating models, we explore a mass range of $30-40 M_\odot$ in increments of $1 M_\odot$ plus our $30.5 M_\odot$, and we test a $50 M_\odot$ & $60 M_\odot$ to mark the hydrogen abundance at relatively higher masses.

Our primary focus is determining any variation of low mass hydrogen envelopes between single and binary systems. Below we describe our model assumptions for each scenario.

#### 2.1.1. *Single Stars*

According to Heger & Langer (2000), rotation enhances mass-loss such that $\dot{M}_{rot} = \dot{M}_{non-rot}/(1 - \Omega/\Omega_{crit})^{0.43}$, where $\dot{M}_{rot}$ is the mass loss of the rotating model and $\dot{M}_{non-rot}$ is the mass loss of the non-rotating model solely due to wind. Furthermore, adequate rotational mixing may lead to the chemically homogeneous evolution seen in massive stars (Heger et al. 2001; de Mink et al. 2009; Chatzopoulos et al. 2012; Yoon et al. 2012). For all rotating models, we adopt a typical rotation velocity for massive stars of $v_{rot} = 200$ kms$^{-1}$. For these rotating models, we similarly explore $30-40 M_\odot$ in increments of $1 M_\odot$, & $45-65 M_\odot$ in increments of $5 M_\odot$.

For both single and binary systems, we assume a few fixed parameters. Namely:

- For our preliminary models, we implement the fiducial nuclear reaction network `approx21_cr60` to model advanced stages of burning. This network extends the basic network describing hydrogen and helium burning by including C/O burning and alpha chains (Timmes 1999). In an effort to reproduce similar core burning conditions at high mass, we adopt the `"CF88"` reaction rate (Caughlan & Fowler 1988) implemented by Sukhbold & Woosley (2014) to study the compactness of pre-SN cores for masses ranging $15-65 M_\odot$. Later we will run our suite of models with the full 204 isotope network (see Table 2). The isotope network allows `MESA` to accurately simulate the moments right before core-collapse. Thus, this particular isotope network is essential to modeling progenitors of CCSN.

- The metallicity of a star drives solar winds determines the star's mass-loss efficiency in non-rotating cases, which can cast the outcome of a CCSN (Trani et al. 2014). High-metallicity stars tend to increase winds and lose more mass than low-metallicity stars (see Figure 5 and Trani et al. 2014). Furthermore, low-metallicity stars tend to deplete more core hydrogen than high-metallicity stars due to raised central burning temperatures and shorter timescales on the main-sequence (Chatzopoulos et al. 2012). We initially prescribe a solar value for metallicity ($Z = 0.014$), and we will explore other values where appropriate in a forthcoming work.

- In general, stellar evolution codes poorly model stellar convective heat transport due to a highly adiabatic region in between the inner and outer envelope (Bonaca et al. 2012). `MESA` and other one-dimensional hydrodynamics codes choose the canonical "Mixing Length Theory" (MLT) to model convection. In MLT, convective eddy sizes are described by $\alpha H_p$, where $\alpha$ is the mixing-length pa-

rameter and $H_p$ is the pressure scale height (see Bonaca et al. 2012). Some have cited a potential mass-dependence of $\alpha$ (Ludwig et al. 1993). For this study we choose the widely-used value of $\alpha_{MLT} = 2.0$ for all masses, and later we will explore $\alpha_{MLT} = 1.5$.

- We also assume the Ledoux criterion for convection, $\nabla_{rad} < \nabla_{ad} + \nabla_{\mu}$, where $\nabla_{rad}$ is the energy transported by radiation and $\nabla_{ad}$ is the adiabatic energy (Paxton et al. 2011, 2013). In this scenario, we include convection due to baryons which is not included in the Schwarzschild criterion. A parameterized semi-convection in terms of $\alpha$ (the mixing length parameter) further resolves convection by defining the efficiency of chemical mixing beyond the core. This has an important effect on future shell hydrogen burning and, ultimately, the shell hydrogen mass at core-collapse (Ding & Li 2014). We increase the $\alpha$ semi-convection value from the default 0.01 to 0.1. This sets the semi-convective diffusion coefficient to a value that's 10% of the radiative one (Sukhbold & Woosley 2014). We treat the convective cells with potential non-zero velocities, and therefore prescribe overshooting regions for H and He core regions and non-burning shell regions. Due to overshooting and baryonic convection, we include the $P_{extra}$ prescription, which accounts for extra pressure at the surface boundary.

- A constant wind-driven mass loss is calculated using the wind scheme from Glebbeek et al. (2009) for massive stars, where the parameter $\eta = \frac{\dot{M} V_{\infty}}{L/c}$, is defined to be the ratio between wind momentum and radiation momentum. We follow the fiducial rate given by Maeder & Meynet (2001) of $\eta = 0.8$.

#### 2.1.2. *Binary Systems*

In addition to single star modules, `MESA` also includes `MESAbinary`, a binary module. `MESAbinary` solves for each star individually with prescribed values of initial masses in `inlist_project`, `inlist1`, and `inlist2`. The `inlist_project` contains information for the binary system as a whole. `inlist1` and `inlist2` contain information specific to each star. As a result, the control parameters used in `inlist1` and `inlist2` are the same prescriptions `MESA` has for single star systems (`MESAstar`). On the other hand, `inlist_project` contains parameters only included in `MESAbinary`.

Kobulnicky & Fryer (2007) predict that in order for two stars to undergo stable mass transfer and avoid a merger event, the mass ratio between the two stars is near unity ($q \equiv M_2/M_1 \sim 1$); however, $q$ may be as low as 0.3 in some instances. This mass ratio constrains the initial orbital separation of the stars: if the stars are too close, the primary star would engulf the secondary while it is still in the primary giant phase (Sabach & Soker 2015; see Figure 7). In this work, we focus our attention toward models where the mass of the primary is equal to the mass of the secondary for simplicity (Tables 3, 4, and 5).

To compute the initial orbit separation, we implement Eggleton's integration for $q = 1$ (Eggleton 1983) using:

$$R_L/a = \frac{0.49q^{2/3}}{0.6q^{2/3} + \ln(1+q^{1/3})} \ , \ 0 < q < \infty. \quad (1)$$

$$\approx \frac{0.44q^{1/3}}{(1+q)^{0.2}} \ , \ 0.1 \leq q \leq 10. \quad (2)$$

where $R_L$ is the effective radius and $a$ is the orbit's semi-major axis. For $q = 1$, we find $R_L/a \sim 0.2$ and the initial orbit separation $\sim 3$ days. In forthcoming work, we will explore the dependence of initial orbit separation on mass.

Following suit of those fixed parameters discussed above in §2.1.1 for single star modules, below we detail a few more fixed parameters for our interacting binary models (see Table 4):

- We use the `Ritter` scheme, which estimates the mass transfer rate when the donor's atmosphere extends past its Roche lobe. In this environment, $R_1 < R_{RL,1}$, where $R_1$ is the donor's radius and $R_{RL,1}$ is the radius of the donor's Roche lobe (Ritter 1988). We do not consider the case when $R_1 > R_{RL,1}$.

- Mass loss in non-rotating binary systems can be due to stellar winds and tides, and may be phase-dependent (e.g. during RLOF; see Vos et al. 2015). We treat mass loss as a simple fraction of mass lost from wind in the vicinity of the acceptor/donor. To simplify calculations, we ignore tidal forces, which, when enhanced by rotation, can change the shape of the star and increase oblateness (Chatzopoulos et al. 2012). Instead, we treat the models as having rigid body rotation. We also treat mass transfer implicitly by iterating the previous solution of mass transfer for the sake of speed of calculation. We include mass loss for radiation-driven winds of hot stars, as prescribed by the `Kudritzki` wind scheme. We set the mass loss wind efficiency to be $\eta = 1.0$ (Kudritzki et al. 1989). We will explore other values of $\eta$ in forthcoming work.

- We include several of the same single-star free parameters, namely: Ledoux criterion, mixing-length $\alpha$, and $\alpha$ semi-convection. In contrast to the single-star suite, however, we reduce the mixing-length $\alpha$ to 1.5. In doing so, we increase the effective radius versus luminosity. We also decrease the $\alpha$ semi-convection from 0.1 to 0.01 to refine the semi-convective diffusion coefficient to a value that's 1% of the radiative one (Sukhbold & Woosley 2014).

- In regions that cannot be resolved by canonical mixing, likely due to an inversion in the mean-molecular weight that creates convective instability ($\nabla_T - \nabla_{ad} \leq B \leq 0$, where $\nabla_T$ is the temperature gradient, $\nabla_{ad}$ is the adiabatic gradient, and $B$ is the Ledoux term), we include thermohaline mixing. We assume a diffusion coefficient of $D_{th} = 1.0$ in line with Charbonnel & Talon 2008.

*Rotating Binary Systems*— Rotation in binary systems is considerably more complicated than single star rotation (Paxton et al. 2015). As a result, we devote a section

to outlining the additional fixed parameters included in our rotating binary models.

- The mechanism that causes material to be lost via rotation in a binary system is not well-understood (Paxton et al. 2015), potentially because rapid winds prohibit mass from accreting onto the donor (Cantiello et al. 2007). Thus, we assume initial orbit synchronization when implementing the default (and arbitrary) value for the surface velocity rotation $v_{rot} = 50$ kms$^{-1}$.

- We include the diffusion of angular momentum and mixing of material as set by Heger & Langer 2000. We set the angular momentum diffusion mixing factor to $L_{mix} = 0.0333$. Due to a non-zero $L$ value, we adopt a non-zero value for the metallicity of the opacity ($Z_{base} = 0.02$).

- Our wind scheme prescription for mass loss differs from the non-rotating binary case because the stars are no longer constrained to the hot star radiative wind regime. Instead, we adopt the WR "Dutch" wind scheme used for massive stars (Glebbeek et al. 2009). The binary system has a higher $\eta$ than the single star case ($\eta_{binary} = 1.0 > \eta_{single} = 0.8$) to reflect enhanced wind interaction between the donor and accretor.

### 2.2. *A Single Star Model Run*

To describe a single star test run, we choose the rotating case of a 40M$_\odot$ star. Initially, we evolve the pre-main sequence star to the main-sequence. Once the luminosity from nuclear burning is 99% of the luminosity (in other words, the star hits ZAMS), we stop the run. At this point, we turn rotation on ($v_{rot} = 200$ kms$^{-1}$) while including a constant mass loss wind scheme as done for single stars. The rotating star then undergoes various stages of nuclear fusion. As mass loss picks up, we track the hydrogen abundance as a function of shell mass. If the star extinguishes all hydrogen before exhausting silicon, we record the hydrogen abundance at the end of the model as 0.00. If the star still retains above $10^{-3}$ M$_\odot$ of hydrogen by the time of core silicon burning, we record that hydrogen abundance.

Once the star extinguishes silicon, we stop the model and save it. At this point, the star encounters periods of episodic mass loss and large jumps in velocities that form shocks. This pre-SN mass loss and episodic shocks are not well understood. Similarly, traditional numerical algorithms that are dependent on the number of threads break down in this regime (Paxton et al. 2011). Thus, the previous `inlist` cannot calculate the large shock velocities, and so in a forthcoming work, we switch to a new `inlist` that breaks the supernova down into steps. It calls upon the saved model and implements `BCYCLIC` (Hirshman et al. 2010), a parallel linear algebra solver optimized for speed. We add a prescription to the `inlist` that injects energy ($E_{inj} = 1.51\times10^{51}$ ergs) at a constant rate (where $E_{inj} > E_{\rm bind}$) onto the pre-SN star to start the SN shock. The energy injection is then halted when $E_{tot} - E_{tot,i} > E_{inj}$. This creates a pressure build-up, forming a shock wave (Mach $\mathcal{M}_c \approx 2$)(see Paxton et al. 2011, 2013).

### 2.3. *A Binary System Model Run*

To examine a `MESAbinary` run, we choose the non-rotating case of a 6M$_\odot$ − 6M$_\odot$ (M$_{tot}$ = 12M$_\odot$) system. We evolve the system from ZAMS by initializing `inlist_project`, `inlist1`, and `inlist2`.

Both the accretor and the donor spend the majority of their lives on the main sequence as the donor gradually loses mass. Once the donor loses enough mass (in this case, $\sim$ 5.14M$_\odot$), the donor progresses to helium fusion. At this point, the accretor undergoes thermohaline mixing throughout the star, while thermohaline mixing in the donor is limited to its outer envelope. Below the envelope, the donor has a fully convective zone that gradually transitions to a radiative one sans mixing. The donor's core regains thermohaline mixing. Once both stars progress through the main sequence, the donor stops losing mass. It continues to fuse helium as the accretor gradually picks up mass. The accretor gains enough mass to stimulate later stages of nuclear fusion, particularly carbon and oxygen. It also re-fills its hydrogen content, maintaining a large amount of hydrogen ($\sim$ 5.90M$_\odot$) throughout most of its composition.

At this point, the time-steps are reduced as the stars undergo complex outer-envelope interactions. `MESA` cannot resolve common envelope or contact binaries (Paxton et al. 2015). Thus, we choose to terminate the run at the onset of oxygen burning.

### 2.4. *Computation of Remnant Hydrogen $M_H^{env}$*

Here, we describe our method of computing of M$_H^{env}$, $X_{surf}$, and $Y_{surf}$. In our single star models, once the star extinguishes silicon, we stop the run. We use the text file `profiles_index` to find the abundance profile that corresponds to the last timestep. The abundance profile plots $m/M_\odot$ versus log mass fraction (see Figures 8, 9, 10, 11). To compute $X_{surf}$, the hydrogen abundance at the surface, we analyze the log mass fraction at the surface of the star ($m/M_\odot \approx 0$). We implement the same method for $Y_{surf}$, the helium abundance at the surface. To compute M$_H^{env}$, the mass of the hydrogen envelope, we integrate the area under the hydrogen curve by rectangular integration. Though trapezoidal integration may be more accurate, the mass fraction is generally so small that any increased accuracy is only on the order of 5%.

We use roughly the same method for binary systems, but with a few variations. The binary models produce two abundance profiles per run, one for the accretor and one for the donor. We analyze each abundance profile separately, and report the results as M$_{H,1}^{env}$ and M$_{H,2}^{env}$. Because these models do not run to core-collapse, we analyze abundance profiles that correspond with the onset of oxygen burning.

## 3. RESULTS

In Table 5 we present results from our `MESA` models of stars with ZAMS masses of 20 − 60M$_\odot$. For our non-rotating models where $\eta = 0.8$, stars with masses below 33M$\odot$ possess more than 0.1M$\odot$ of hydrogen on their surface, while models between 34 − 36M$\odot$ retain less by an order of magnitude. When we increase $\eta$ to 1.0, the range of masses that keep trace amounts of hydrogen tend to shift toward lower values in log T$_{eff}$. A similar

effect is seen for our rotating models that assume $\eta = 0.8$. Plotted in Figure $8 - 11$ are elemental abundance profiles near core-collapse for several non-rotating models.

In Figure 12, we plot the mass of surface hydrogen on an HR diagram for all model runs. Red and blue circles denote when a star is semi-stripped or fully-stripped of its surface hydrogen, respectively. Smaller circles symbolize that the mass of the star's remaining hydrogen envelope is relatively less by an order of magnitude. Ultimately, semi-stripped stars will produce H$\alpha$ in the CCSN spectra, while fully-stripped models will produce signatures of Si II $\lambda$6355 upon explosion.

Overall, our fully-stripped stars tend toward higher $\log T_{eff} > 5.6$ and are slightly more luminous than our semi-stripped stars. The fully-stripped stars also appear to congregate along an asymptote, while the semi-stripped models span $3.8 < \log T_{eff} < 5.3$ and occupy a narrow extent in $\log L/L_{\odot}$ up to 5.9.

For our suite of non-rotating models, overall differences in the assumed value of $\eta$ are slight. When the wind is parameterized by $\eta = 0.8$, more semi-stripped stars are produced than for $\eta = 1.0$. In addition, a higher value of $\eta$ effectively lowers the maximum ZAMS mass giving rise to stars with more massive hydrogen envelope (i.e. $M_H > 1.0 M_{\odot}$). Adding rotation further decreases the occurrence of stars between $30 - 55 M_{\odot}$ that retain trace amounts of hydrogen.

For our binary suite (see Table 6), we find certain combinations of masses are also capable of leaving trace amounts of hydrogen that is just above estimated mass thresholds for SN Ib ($\sim 10^{-3}$ $M_{\odot}$) and just under that for SN IIb ($10^{-2}$–$10^{-1}$ $M_{\odot}$). However, the output values for these exploratory models are left for additional analysis before sound interpretations can made.[3]

Still, we are able to consider two possible preliminary interpretations should this amount of remnant hydrogen remain fixed. Assuming the close binary systems avoid a merger, there will be a large amount of leftover hydrogen on the secondary star ($\sim M_H > 1.5 M_{\odot}$). This would effectively rule out the system as a SN Ib progenitor. However, if observations reveal evidence of angle-dependent effects (so far, they have not), then we must consider the possibility that they lead to some SN Ib. If, on the other hand, the stars do merge, to coincide with observations of faint $H\alpha$ in SN Ib spectra the binary product (donor plus accretor) must shed the secondary's re-filled hydrogen content via either constant wind or violent episodic eruptions.

Application of our single star models to specific observations is carried out with a comparison to the SN Ib iPTF13bvn, where a progenitor has been identified from pre-SN archival images (Cao et al. 2013). A Wolf-Rayet progenitor system was deemed reasonable by Cao et al. (2013), while models done later by Groh et al. (2013) favored a single star channel with a ZAMS mass of $32 M_{\odot}$. Modeling done by Fremling et al. (2014) later disfavored the Wolf-Rayet channel for iPTF13bvn. Interestingly, Eldridge et al. (2015) recently found that the photometry of Cao et al. (2013) underestimates the apparent brightness of iPTF13bvn, thereby placing the luminosity of the candidate progenitor to be in excess of initial values by $0.2 - 0.7$ mag. From evolutionary calculations of binary stars, Eldridge et al. (2015) also find binary systems cannot be ruled out for iPTF13bvn.

In our Figure 12, the approximate location of iPTF13bvn on the HR diagram is indicated by a dashed box. Overall, the closest models to this region have hydrogen envelope masses less than a solar mass, with ZAMS masses spanning $27 - 33 M_{\odot}$; apart from lacking surface hydrogen, none of the fully-stripped models are close enough on the HR diagram to be associated with this particular SN Ib. All of our semi-stripped models may represent some SN Ib observed in nature, however it is our rotating $32 M_{\odot}$ model that is closest to the putative position of iPTF13bvn. In a forthcoming work, we will expand the explored parameter space in order to see if a $32 M_{\odot}$ progenitor can be uniquely favored for iPTF13bvn.

## 4. SUMMARY AND CONCLUSIONS

In this study, we evolved a suite of $20 - 60 M_{\odot}$ rotating and non-rotating models of solar metallicity to understand the impact of mass loss (both rotationally induced and wind-driven) on the last remaining amount of hydrogen on the star's surface. Depending on the value of $\eta$, we see that the amount of hydrogen retained decreases by an order of magnitude over this mass range (see Table 5).

Overall, the amount of surface-layer hydrogen removed by a stellar wind is found to be positively correlated with the amount of surface-layer hydrogen removed by stellar wind, which can be enhanced by effects of rotation. In the case of a line-driven wind, mass can be increased further with an increase in the progenitor's metallicity. Under an asymmetric stripping mechanism, as may be the case for some binary scenarios and fast-rotating stars, or should an outer envelope be lost in discrete and violent phases of mass loss, thresholds of the mass lost by a stellar system can be over-estimated from first principles of a constant and spherically symmetric wind.

Consequently, we do not consider our finding as well-determined. Rather, we have explored how one might utilize evolutionary models and post-explosion signatures of faint H$\alpha$ to rule out fully-stripped progenitor systems of core-collapse supernovae while simultaneously constraining abundances of freshly synthesized material.

According to mass estimates obtained from spectrum synthesis calculations for supernovae (e.g., James & Baron 2010), the amount of surface hydrogen on the progenitor, namely, $M_H = 1.0$, 0.1, and 0.01, is approximately consistent with a supernova association of SN II, IIb, and Ib, respectively, i.e., the exact mass threshold for SN IIb and Ib is uncertain by an order of magnitude. For SN Ic, like SN 1994I, with faint signatures of H$\alpha$ shown in Figure 3, we suspect the mass of surface hydrogen on the progenitor is closer to $0.001 M\odot$ or less. In terms of a mass sequence, this would imply that SN Ic, as well as other events that are truly devoid of detectable H$\alpha$ ("SN Id"), originate from progenitors that are more massive than those for SN II, IIb, and Ib.

Another promising result found here (see also Groh et al. 2013) is that the candidate progenitor system iden-

[3] We also ran a suite of rotating binary models, but do not report our initial results. We run into a number of problems in the rotating binary regime; namely that the system remains "stuck" on the main sequence (for example, our $10 M_{\odot} - 10 M_{\odot}$ system took $\sim 10^7$ years) without losing a significant amount of mass and/or hydrogen. We suspect that we do not treat the mass loss scheme properly, and will explore this in future work.

tified for SN Ib iPTF13bvn is most consistent with a $32M_{\odot}$ star that has been stripped of all but less than $0.06M_{\odot}$ of its surface hydrogen. We therefore suspect a signature of faint H$\alpha$ will be produced in future spectrum synthesis calculations during the post-explosion evolution (cf. Dessart et al. 2011, 2012). Our study thus highlights the importance of high cadence follow-up spectroscopy of all semi-stripped and fully-stripped events, as well as pre-SN imagining and stellar evolutionary modeling most useful for constraining progenitor models of SN IIb, Ib, Ic, and "Id".

In summary:

- We find models that are in the vicinity of iPTF13bvn.

- We determine that using hydrogen as a free parameter, whether or not it's detected, can help constrain the properties of the progenitor ($T_{eff}$, luminosity, mass, rotation, etc).

## 5. FUTURE WORK

Some outstanding questions remain, including:

- The mass sequence of semi-stripped versus fully-stripped models is not linear. For each suite of rotating and non-rotating models considered, one semi-stripped star stands out from fully-stripped stars along similar mass ranges. Between rotating and non-rotating models that assume $\eta = 0.8$, the lone semi-stripped star has a ZAMS of $40M_{\odot}$. It is unclear if this is an artifact of our prescribed stellar evolution (i.e. our assumed `inlist` parameters), or if this effect is truly a consequence of underlying physics not addressed in this work.

- For our non-rotating models that assume $\eta = 1.0$, stars with ZAMS $> 41M_{\odot}$ leave less than $0.5M_{\odot}$ in the outermost $3M_{\odot}$ of the star. Are these the progenitors of SN Ic?

- Other types of supernovae where signatures of H$\alpha$ have been debated are broad-lined SN Ic, gamma-ray bursts, super-luminous supernova of type I, in addition to faint and fast-evolving SN Ib/c. Where are the progenitor systems for these if all have detectable traces of hydrogen?

In an effort to resolve these unknowns, we will tabulate results from an extended parameter space in a forthcoming work.

*Acknowledgements.* It is a pleasure to thank Dr. Jerod Parrent and Dr. Alicia Soderberg for their invaluable guidance and stimulating discussions. This work is supported in part by the National Science Foundation REU and Department of Defense ASSURE programs under NSF Grant no. 1262851 and by the Smithsonian Institution.

## REFERENCES

Bonaca, A., et al. 2012, ApJ, 755, L12
Cantiello, M., Yoon, S.-C., Langer, N., & Livio, M. 2007, A&A, 465, L29
Cao, Y., et al. 2013, ApJ, 775, L7
Caughlan, G. R., & Fowler, W. A. 1988, Atomic Data and Nuclear Data Tables, 40, 283
Charbonnel, C., & Talon, S. 2008, in IAU Symposium, Vol. 252, IAU Symposium, ed. L. Deng & K. L. Chan, 163–174
Chatzopoulos, E., Robinson, E. L., & Wheeler, J. C. 2012, ApJ, 755, 95
Crowther, P. A. 2007, ARA&A, 45, 177
de Mink, S. E., Cantiello, M., Langer, N., Pols, O. R., Brott, I., & Yoon, S.-C. 2009, A&A, 497, 243
Dessart, L., Blondin, S., Hillier, D. J., & Khokhlov, A. 2014, MNRAS, 441, 532
Dessart, L., Hillier, D. J., Li, C., & Woosley, S. 2012, MNRAS, 424, 2139
Dessart, L., Hillier, D. J., Livne, E., Yoon, S.-C., Woosley, S., Waldman, R., & Langer, N. 2011, MNRAS, 414, 2985
Ding, C. Y., & Li, Y. 2014, MNRAS, 438, 1137
Eggleton, P. P. 1983, ApJ, 268, 368
Eldridge, J. J., Fraser, M., Maund, J. R., & Smartt, S. J. 2015, MNRAS, 446, 2689
Filippenko, A. V. 1988, Proceedings of the Astronomical Society of Australia, 7, 540
—. 1997, ARA&A, 35, 309
Filippenko, A. V., Porter, A. C., & Sargent, W. L. W. 1990, AJ, 100, 1575
Fremling, C., et al. 2014, A&A, 565, A114
Glebbeek, E., Gaburov, E., de Mink, S. E., Pols, O. R., & Portegies Zwart, S. F. 2009, AAP, 497, 255
Groh, J. H., Georgy, C., & Ekström, S. 2013, A&A, 558, L1
Heger, A., & Langer, N. 2000, ApJ, 544, 1016
Heger, A., Woosley, S. E., Martínez-Pinedo, G., & Langanke, K. 2001, ApJ, 560, 307
Hirshman, S. P., Perumalla, K. S., Lynch, V. E., & Sanchez, R. 2010, Journal of Computational Physics, 229, 6392
James, S., & Baron, E. 2010, ApJ, 718, 957
Jeffery, D. J., Branch, D., Filippenko, A. V., & Nomoto, K. 1991, ApJ, 377, L89
Kobulnicky, H. A., & Fryer, C. L. 2007, ApJ, 670, 747
Kudritzki, R. P., Pauldrach, A., Puls, J., & Abbott, D. C. 1989, A&A, 219, 205
Ludwig, H.-G., Jordan, S., & Steffen, M. 1993, in Astronomische Gesellschaft Abstract Series, Vol. 9, Astronomische Gesellschaft Abstract Series, ed. G. Klare, 147
Maeder, A., & Meynet, G. 2001, A&A, 373, 555
Matheson, T., Filippenko, A. V., Li, W., Leonard, D. C., & Shields, J. C. 2001, AJ, 121, 1648
Minkowski, R. 1941, PASP, 53, 224
Modjaz, M., et al. 2014, AJ, 147, 99
Nugent, P. E., et al. 2011, Nature, 480, 344
Parrent, J. T., Milisavljevic, D., Soderberg, A. M., & Parthasarathy, M. 2015, arXiv:1505.06645
Paxton, B., Bildsten, L., Dotter, A., Herwig, F., Lesaffre, P., & Timmes, F. 2011, ApJS, 192, 3
Paxton, B., et al. 2013, ApJS, 208, 4
—. 2015, arXiv:1506.03146
Pereira, R., et al. 2013, A&A, 554, A27
Pun, C. S. J., et al. 1995, ApJS, 99, 223
Ritter, H. 1988, A&A, 202, 93
Sabach, E., & Soker, N. 2015, ApJ, 806, 73
Sanders, N. E., et al. 2014, arXiv:1404.2004
Smartt, S. J. 2015, PASA, 32, 16
Smith, N. 2015, in Astrophysics and Space Science Library, Vol. 412, Astrophysics and Space Science Library, ed. J. S. Vink, 227
Sukhbold, T., & Woosley, S. E. 2014, ApJ, 783, 10
Taddia, F., et al. 2012, A&A, 545, L7
Timmes, F. X. 1999, ApJS, 124, 241
Trani, A. A., Mapelli, M., & Bressan, A. 2014, MNRAS, 445, 1967
Vos, J., Østensen, R. H., Marchant, P., & Van Winckel, H. 2015, A&A, 579, A49
Wheeler, J. C., Harkness, R. P., Khokhlov, A. M., & Hoeflich, P. 1995, Phys. Rep., 256, 211
Yoon, S.-C. 2015, PASA, 32, 15
Yoon, S.-C., Dierks, A., & Langer, N. 2012, A&A, 542, A113

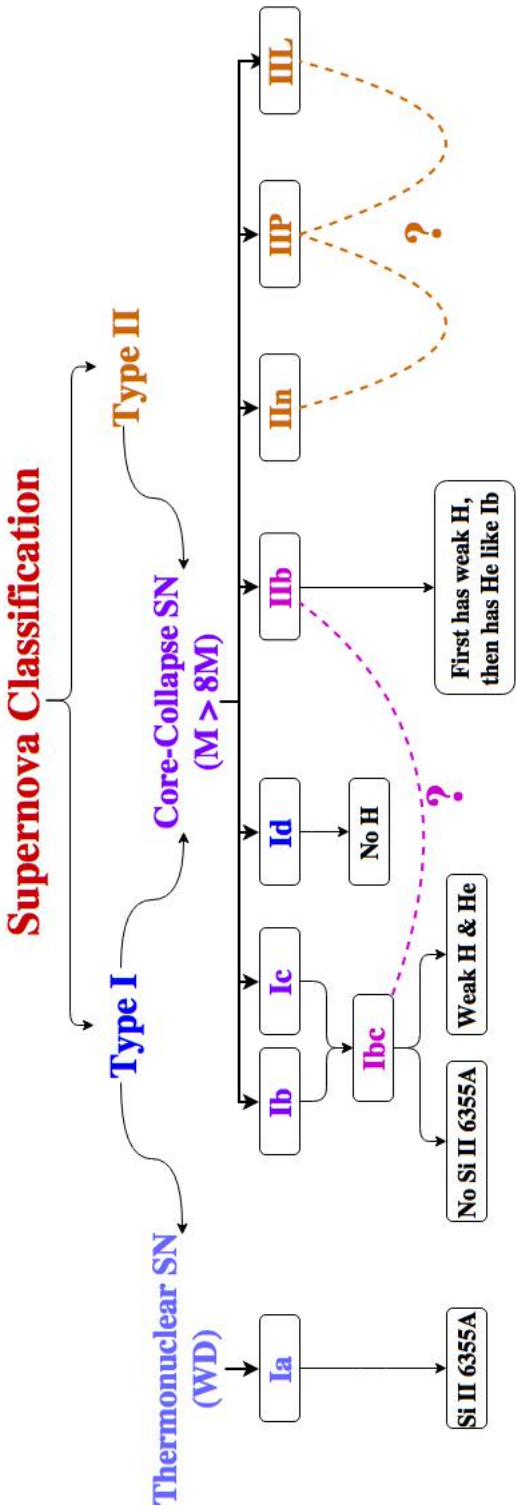


**Figure 1.** Tree diagram of supernova classifications and spectral sequences. SN I result from thermonuclear explosions of white dwarfs (either as a binary system or alongside a compact companion) and are believed to be deficient in detectable hydrogen. By constrast, SN II result from the death of massive, hydrogen-rich progenitor systems. The colors correspond to subclassifications of SN; bluish are Type I and redish are Type II. Light blue corresponds to SN Ia, purple corresponds to SN Ib/Ic, and dark blue corresponds to SN Id. Type II are subdivided into orange (SN IIn, IIP, IIL) and pink (SN IIb). We made both SN Ibc and SN IIb pink to represent a possible connection between the two; namely, that SN IIb tend to resemble SN Ib late in their evolution. This is represented by the dotted pink line. We also connect SN IIn, IIP, and IIL by a dotted orange line to show a possible connection between the three.

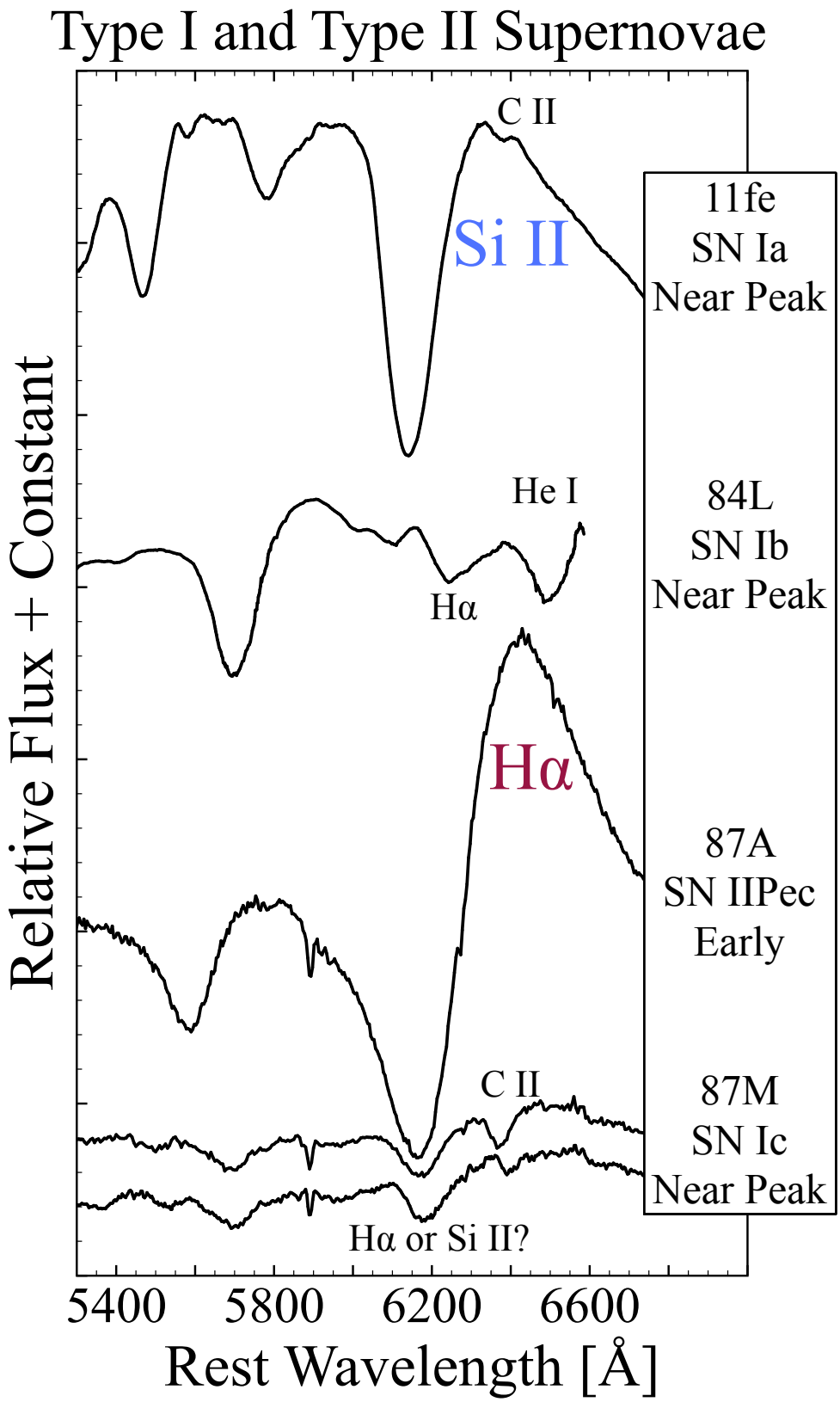


**Figure 2.** Figure and caption from Parrent et al. 2015. Zooming in on Fig. 1 of Filippenko (1997) after a relabeling of features. Spectrum references: SN 1987A soon after the explosion on UT February 24, 1987 (Pun et al. 1995); the spectra for SN 1984L (Filippenko 1997), SN 1987M (Filippenko et al. 1990; Jeffery et al. 1991), and SN 2011fe (Pereira et al. 2013) are near peak brightness.

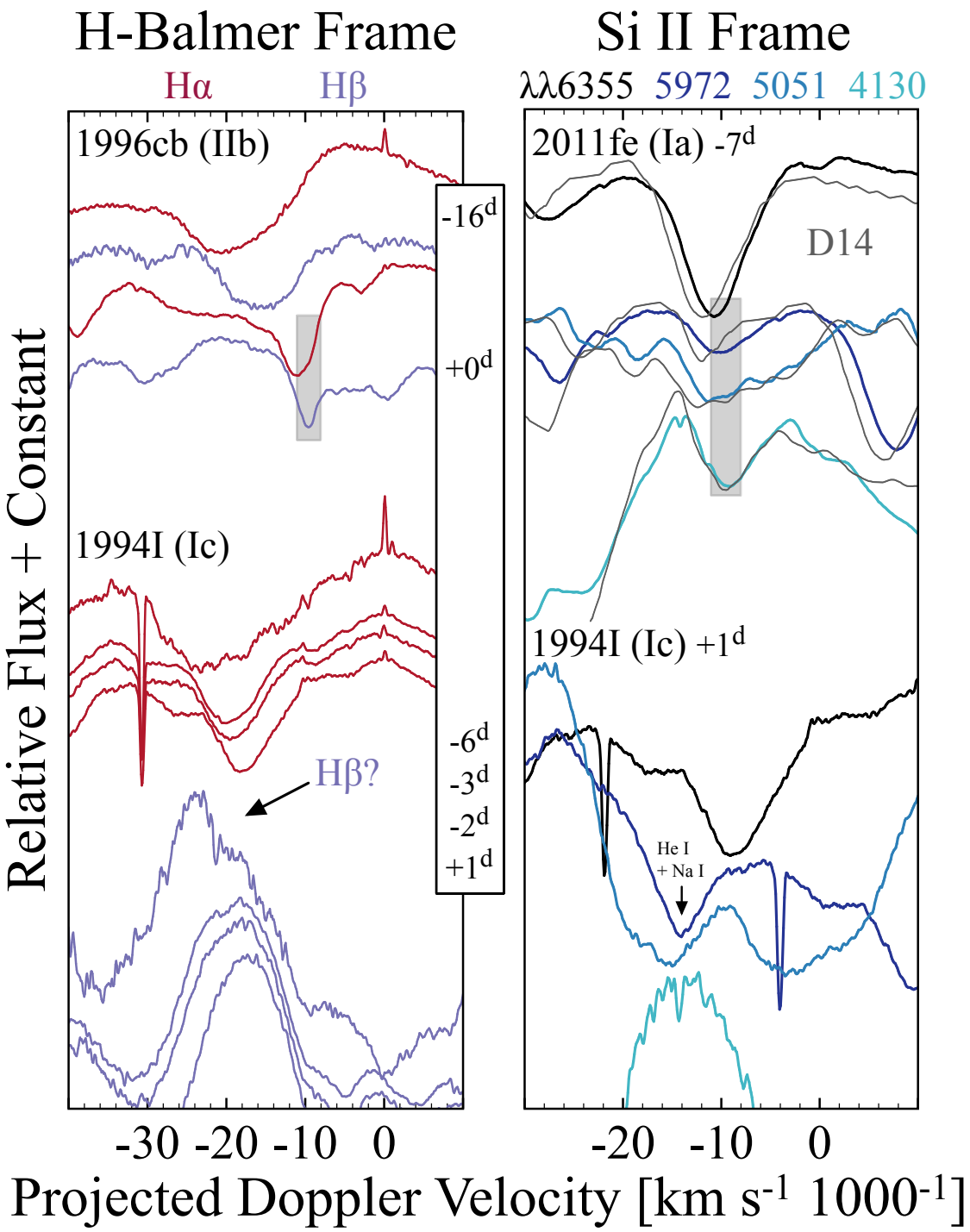


**Figure 3.** Figure and caption from Parrent et al. 2015. Plotted above are project Doppler velocities in the frame of the most likely detectable H-Balmer lines (left) and Si II lines (right). The grey bands are meant to indicate the overlap between common signatures of a given ion. Spectrum references: SN 1994I (Modjaz et al. 2014); SN 1996cb (Matheson et al. 2001); SN 2011fe (Pereira et al. 2013). Model references: (D14) PDDEL4, day −6.6 for SN 2011fe by Dessart et al. (2014).

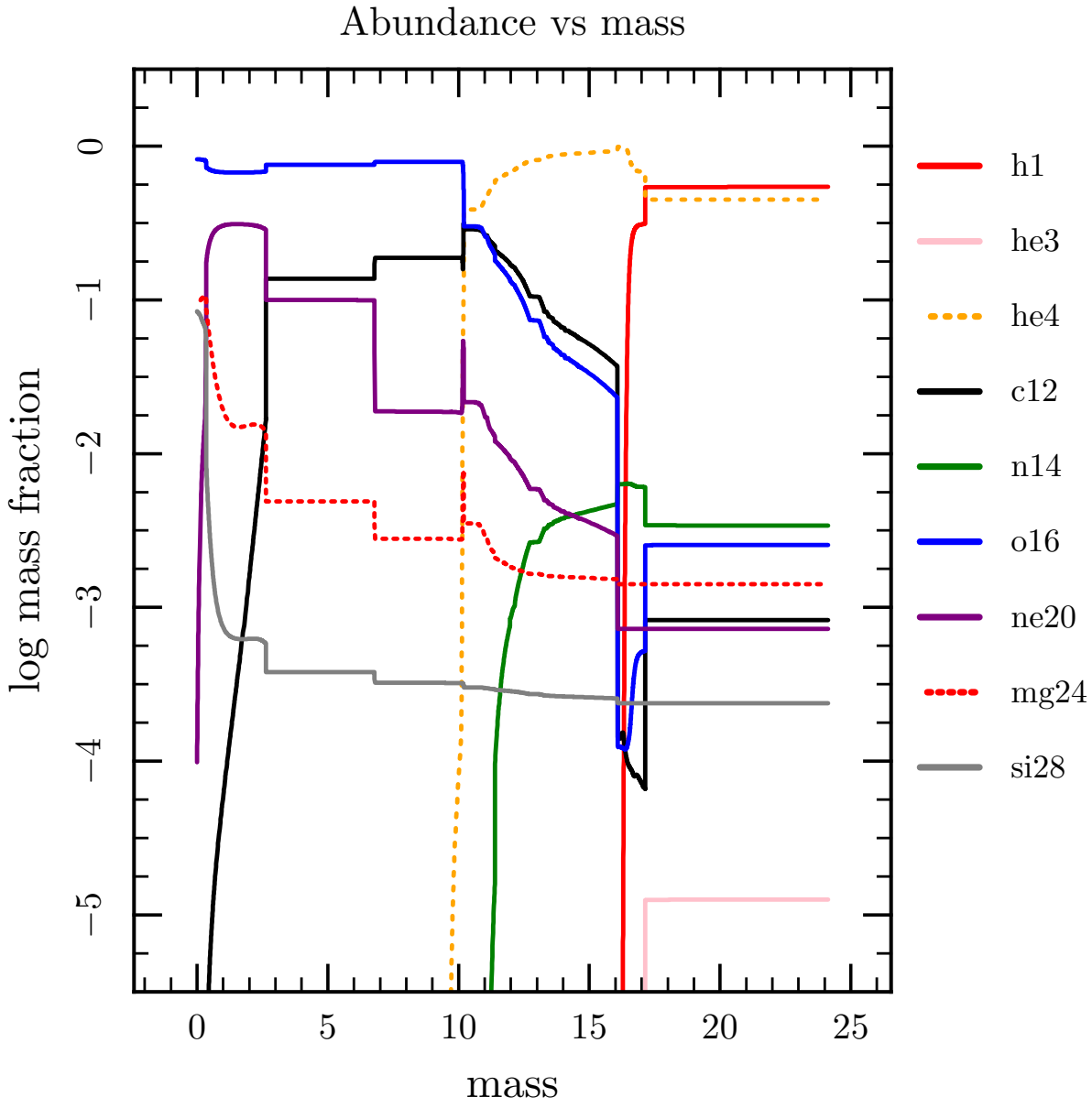


**Figure 4.** Figure from Paxton et al. 2015. Abundances profile for a $40M_{\odot}$ star near core collapse as a function of stellar mass coordinate. Note: if this star blows up before losing several solar masses of its remaining hydrogen envelope, then the spectrum will most likely resemble that of a SN II, and will conflict with the mass of hydrogen detected for SN IIb by a factor of 10 and SN Ib/Ic by a few orders of magnitude.

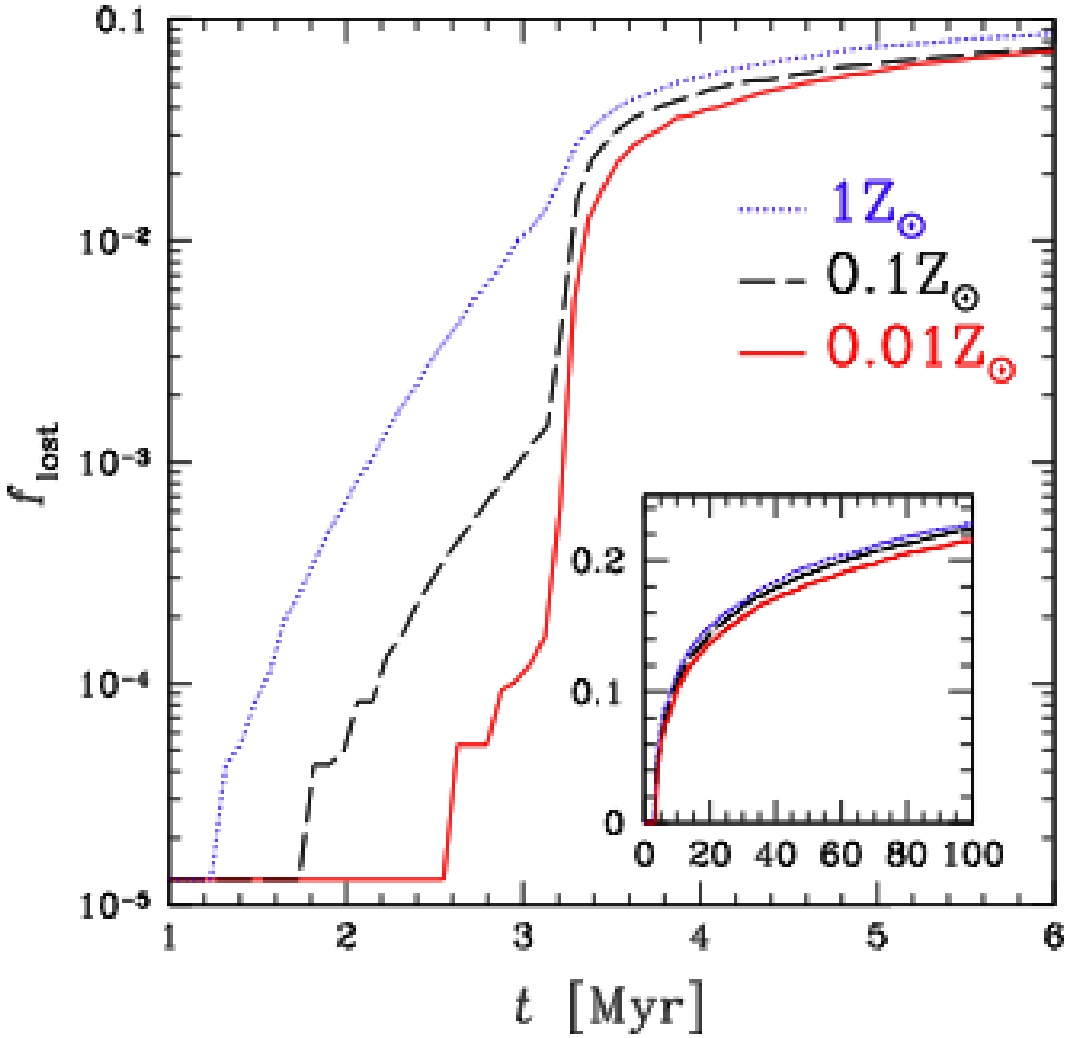


**Figure 5.** Figure and caption from Trani et al. (2014). Cumulative mass loss by stellar winds and SN normalized to the initial mass of the SC as a function of time for three different metallicities. Solid red line: Z = $0.01Z_\odot$ ; dashed black line: Z = $0.1Z_\odot$; dotted blue line: $Z = 1Z_\odot$. Each line is the median value of 10 simulated SCs for different metallicity.

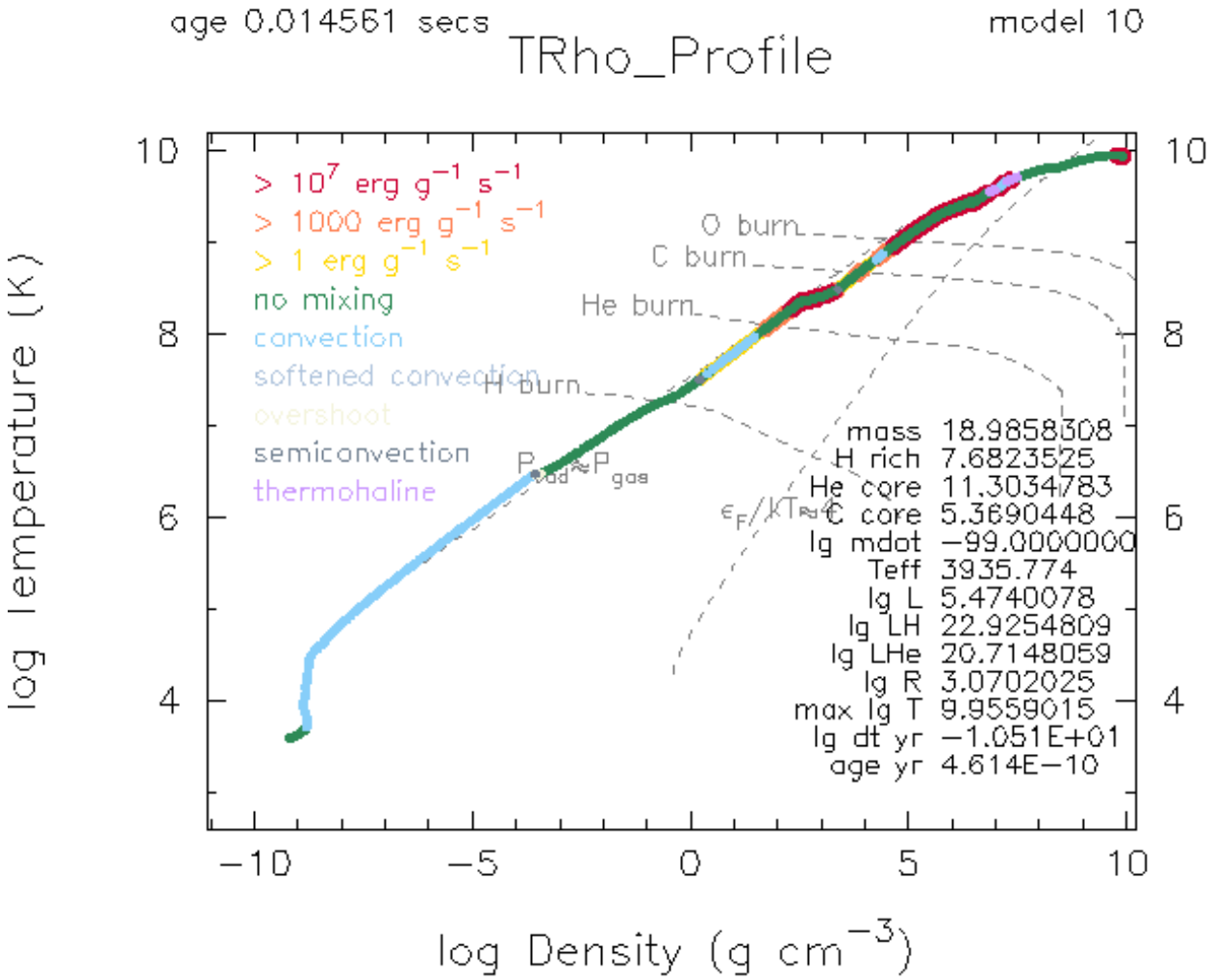


**Figure 6.** Temperature-density still frame of our 31 $M_\odot$ near core collapse. The outer envelope of the star is radiative, and then gives way to a fully convective region. This still was taken extremely near core collapse, when the star has lost $\sim 12.1$ $M_\odot$. We focus solely on the diagonal line where $P_{rad} = P_{gas}$.

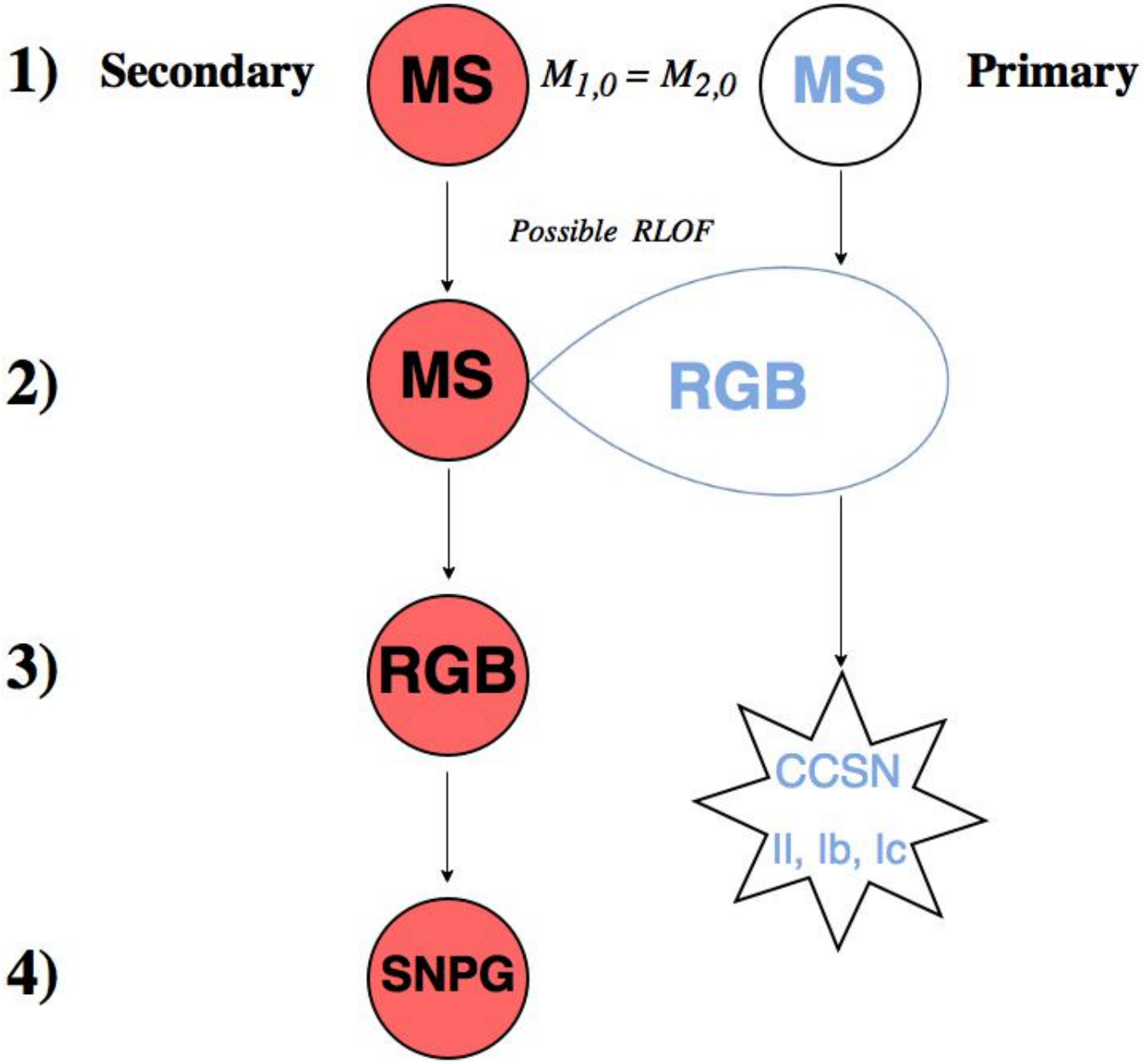


**Figure 7.** We show a schematic of the evolution of a binary system in which q=1 ($M_1 = M_2$). The accretor is in red, while the donor is clear. In (1), both stars begin at ZAMS. In (2), the donor swells onto the red giant branch and begins to transfer mass onto the accretor. At this point, the donor may undergo Roche lobe overflow. In (3), the donor explodes as a SN II/Ib/Ic as the accretor ascends the red giant branch (RGB). In (4), the SN pollutes the RGB, creating a supernova-polluted giant (Sabach & Soker 2015).

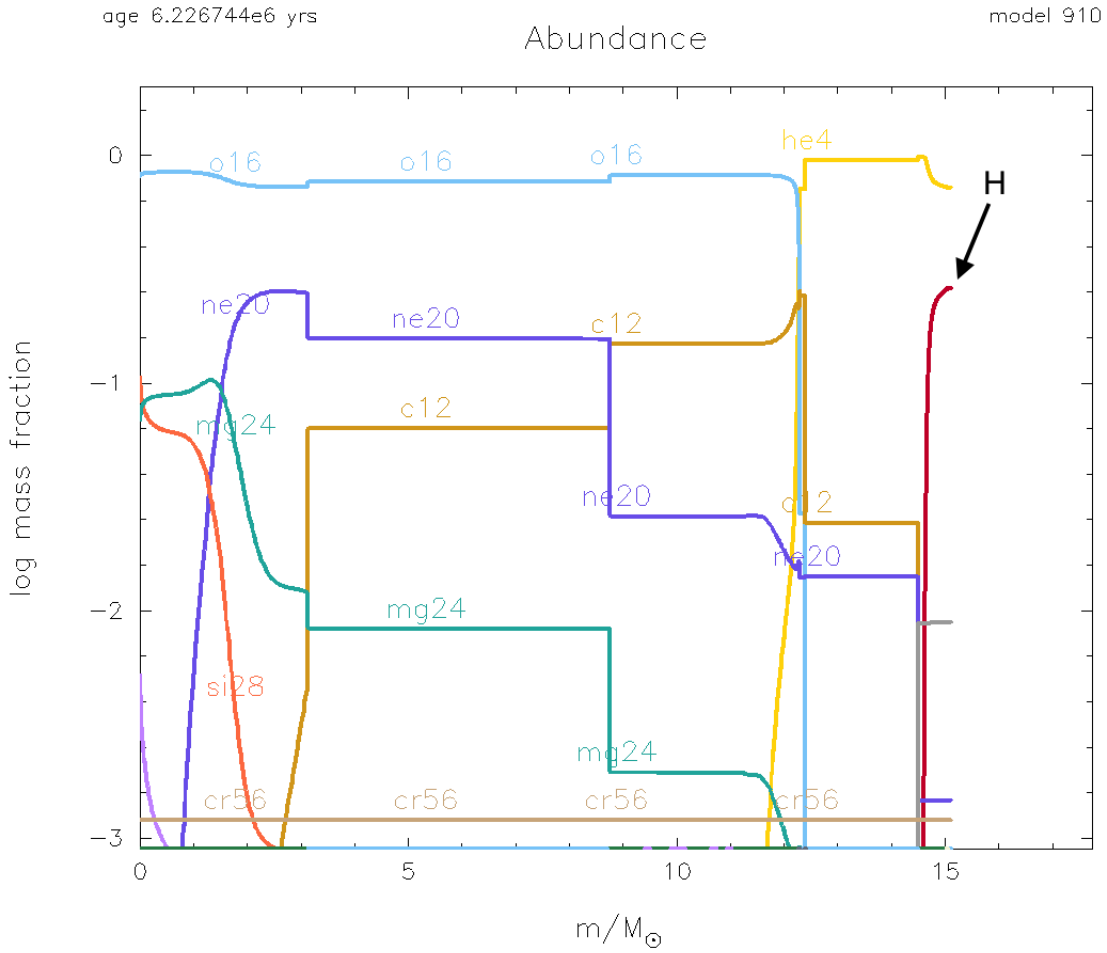


**Figure 8.** Abundances near core-collapse for our non-rotating $32M_{\odot}$ model with $\eta = 0.8$. The mass of the remaining hydrogen is approximately less than $0.1M_{\odot}$.

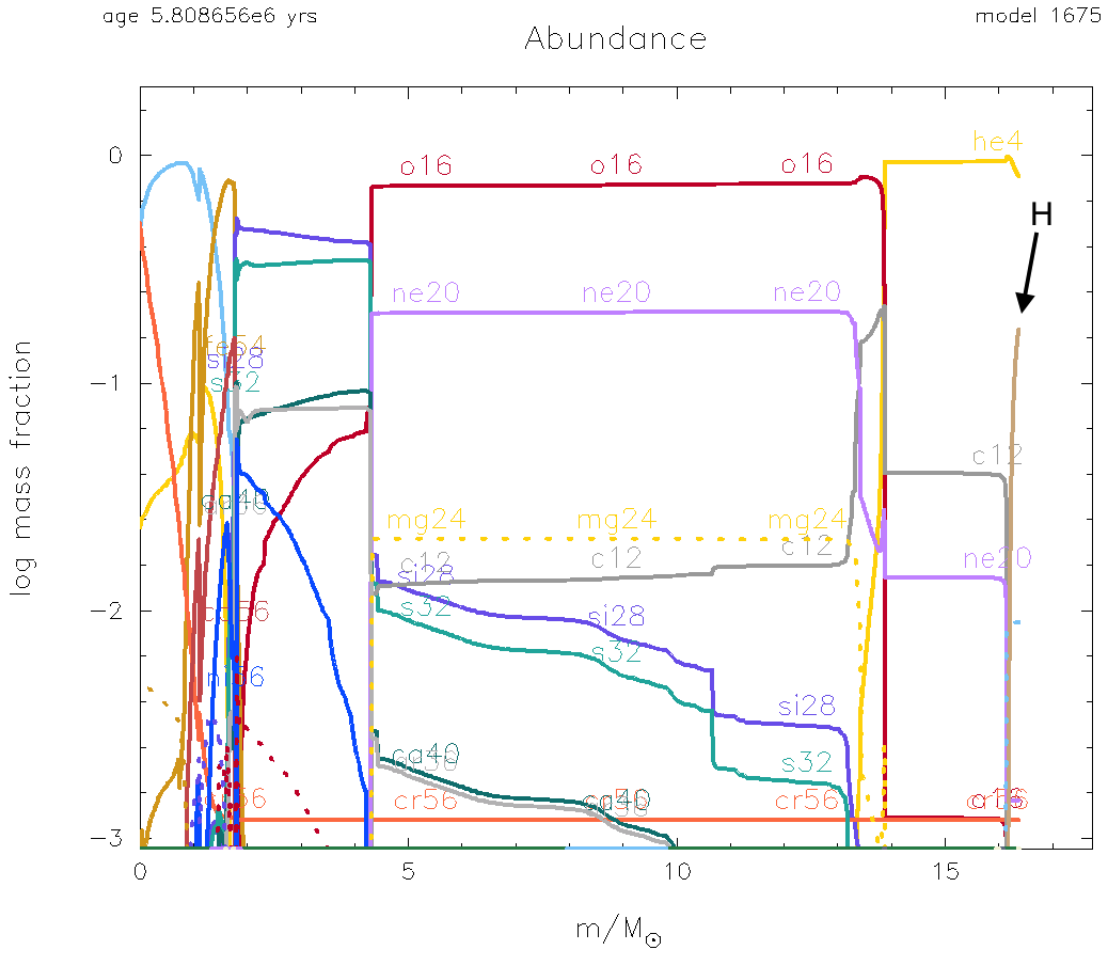


**Figure 9.** Same as Figure 8 but for our 35$M_\odot$ model in the same series. The mass of the remaining hydrogen is approximately less than 0.02$M_\odot$.

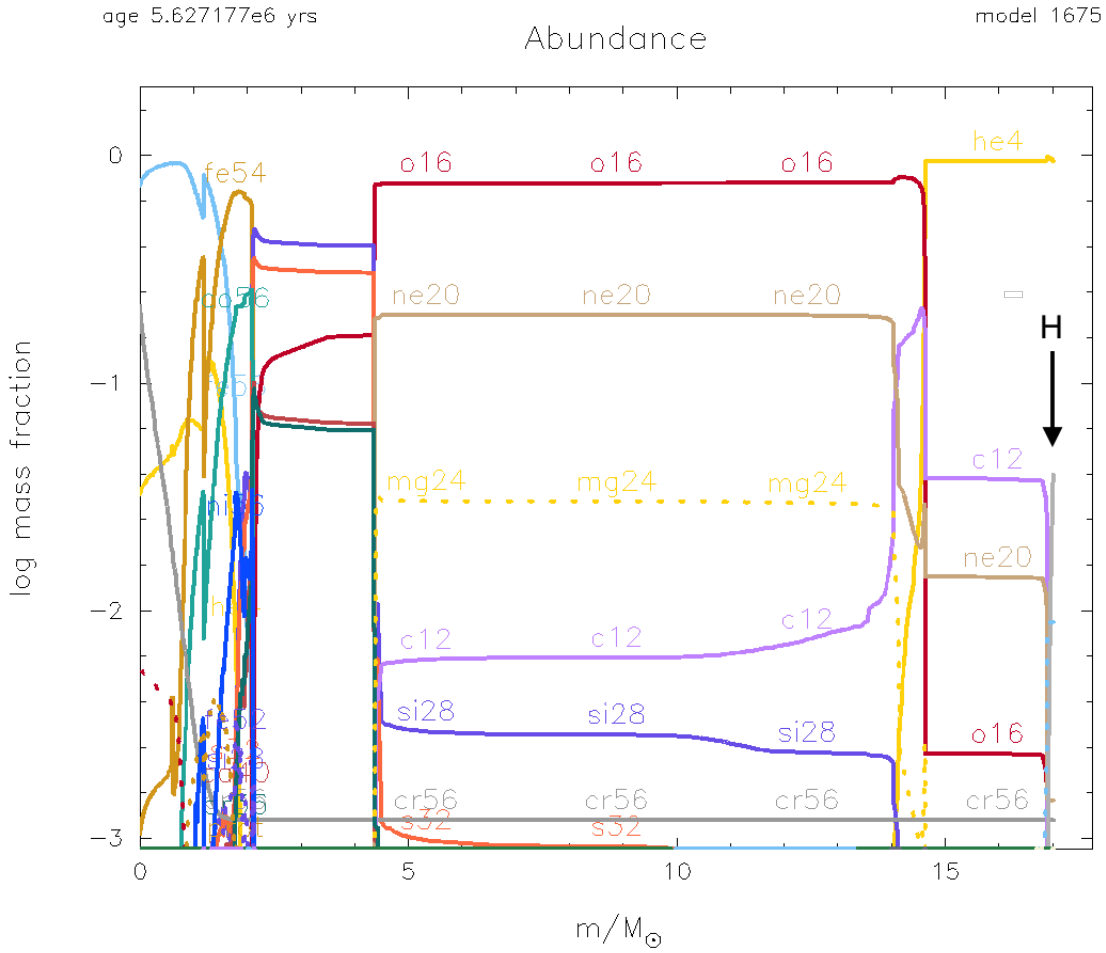


**Figure 10.** Same as Figure 8 but for our 36.5$M_\odot$ model in the same series. The mass of the remaining hydrogen is approximately less than 0.005$M_\odot$.

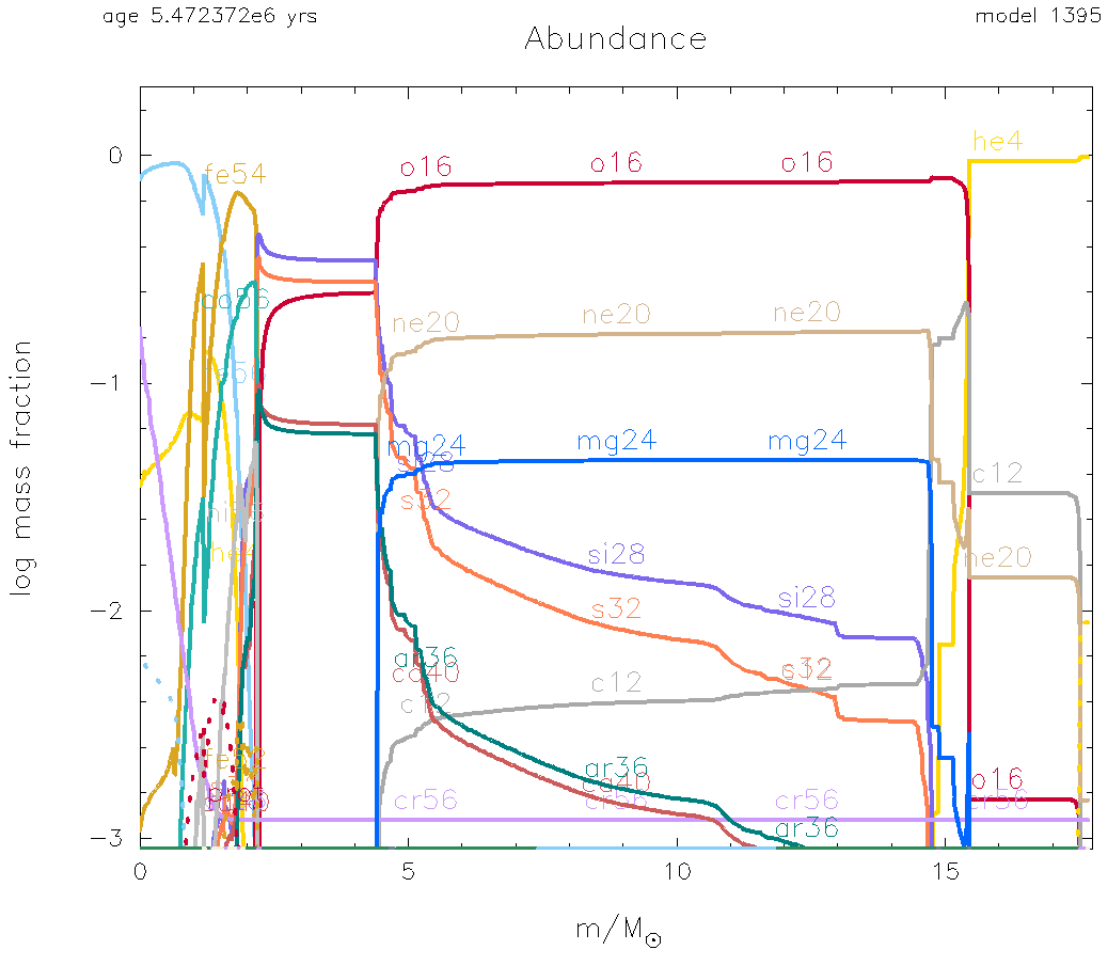


**Figure 11.** Same as Figure 8 but for our 38$M_\odot$ model in the same series. The mass of the remaining hydrogen is approximately less than 0.000$M_\odot$.

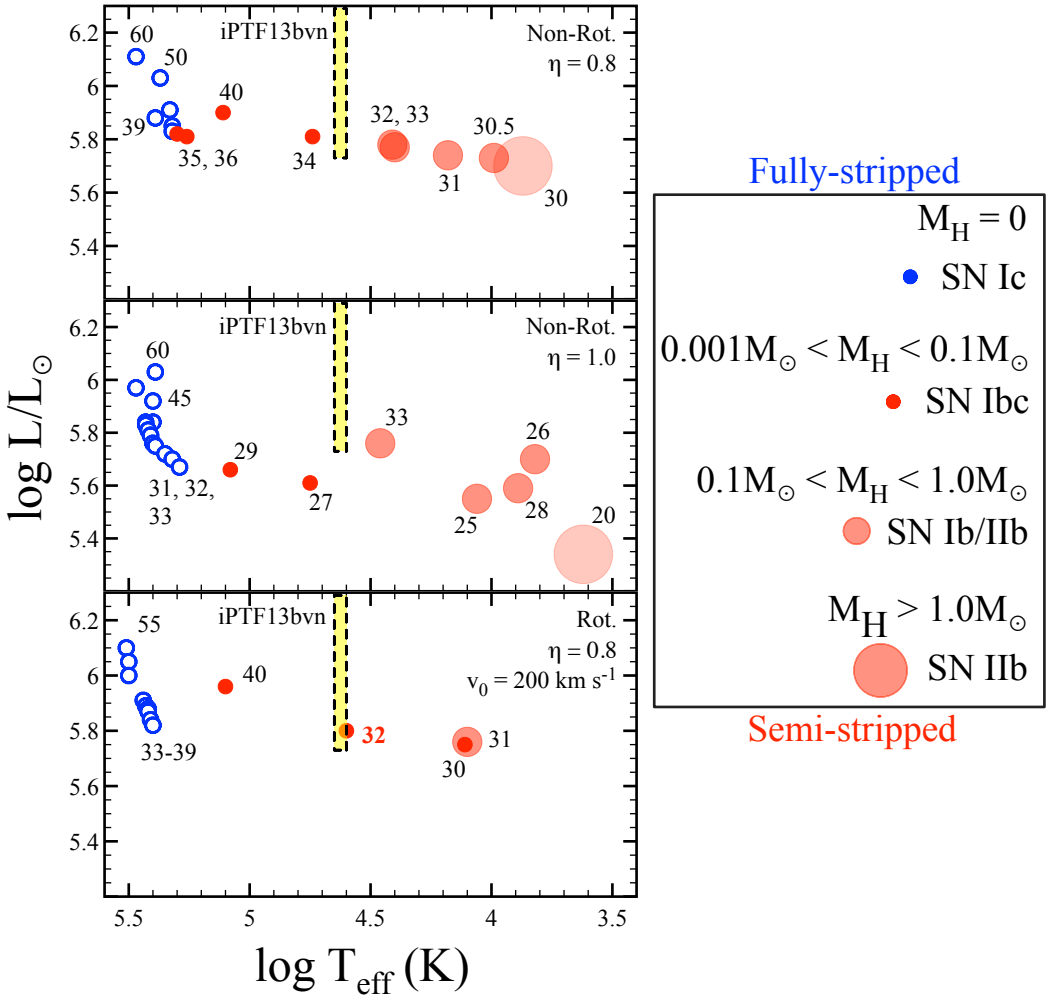


**Figure 12.** A summary of our MESA predictions plotted on an HR diagram and compared to the putative values of iPTF13bvn (dashed box). See legend (right panel) for details.

**Table 1**
Spectral Sequence of Hydrogen Envelope Mass.

| IIP/IIL | IIb | Ib/Ic |
|---|---|---|
| $\sim 5$ $M_\odot$ | $10^{-2}$–$10^{-1}$ $M_\odot$ | $\sim 10^{-3}$ $M_\odot$ |

**Table 2**
204 Isotope Network Listing.

| Element | $A_{min}$ | $A_{max}$ | Element | $A_{min}$ | $A_{max}$ |
|---|---|---|---|---|---|
| n | | | S | 31 | 37 |
| H | 1 | 2 | Cl | 37 | 38 |
| He | 3 | 4 | Ar | 35 | 41 |
| Li | 6 | 7 | K | 39 | 44 |
| Be | 7 | 10 | Ca | 39 | 49 |
| B | 8 | 11 | Sc | 43 | 51 |
| C | 12 | 13 | Ti | 43 | 54 |
| N | 13 | 16 | V | 47 | 56 |
| O | 15 | 19 | Cr | 47 | 58 |
| F | 17 | 20 | Mn | 51 | 59 |
| Ne | 19 | 23 | Fe | 51 | 66 |
| Na | 21 | 24 | Co | 55 | 67 |
| Mg | 23 | 27 | Ni | 55 | 68 |
| Al | 25 | 28 | Cu | 59 | 66 |
| Si | 27 | 33 | Zn | 59 | 66 |
| P | 30 | 34 | | | |

[a]`MESA`'s 204 isotope network listing, courtesy of Bill Paxton.$A$ is the number of nucleons.

**Table 3**
Single Star Free Parameters

| Version | Total Mass | Rotation | Wind |
|---|---|---|---|
| Non-Rotating | 30–37 $M_\odot$ | 0 km $s^{-1}$ | Dutch $\eta = 0.8$ |
| | 40–60 $M_\odot$ | | Dutch $\eta = 1.0$ |
| Rotating | 30–40 $M_\odot$ | 200 km $s^{-1}$ | Dutch $\eta = 0.8$ |
| | 45–65 $M_\odot$ | | |

**Note**. — The single star free parameters in a suite of rotating and non-rotating models.

**Table 4**
Binary System Free Parameters

| Version | Total Mass | Rotation | Wind |
|---|---|---|---|
| Non-Rotating | 8–20 $M_\odot$ | 0 km $s^{-1}$ | Kudritzki $\eta = 1.0$ |
| Rotating | 8–20 $M_\odot$ | 50 km $s^{-1}$ | Dutch $\eta = 1.0$ |

**Note**. — The binary system free parameters in a suite of rotating and non-rotating models.

**Table 5**
Surface Hydrogen Abundance for 20−60 $M_\odot$ Models

| $M_{initial}$ ($M_\odot$) | $M_{final}$ ($M_\odot$) | $M_H^{env}$ ($M_\odot$) | $X_{surf}$ | $Y_{surf}$ | log$L/L_\odot$ | log$T_{eff}$ (K) | Model Conditions |
|---|---|---|---|---|---|---|---|
| 30 | 15.2 | 1.296 | 0.59 | 0.40 | 5.70 | 3.87 | |
| 30.5 | 14.5 | 0.210 | 0.38 | 0.59 | 5.73 | 3.99 | |
| 31 | 14.7 | 0.168 | 0.27 | 0.70 | 5.74 | 4.18 | |
| 32 | 15.1 | 0.098 | 0.26 | 0.72 | 5.77 | 4.40 | Non-rotating Models |
| 33 | 15.5 | 0.137 | 0.25 | 0.74 | 5.78 | 4.41 | $Z = Z_\odot$; $v_{rot} = 0$ km s$^{-1}$ |
| 34 | 16.0 | 0.039 | 0.24 | 0.75 | 5.81 | 4.74 | "Dutch Wind Scheme" ($\eta = 0.8$) |
| 35 | 16.4 | 0.014 | 0.17 | 0.81 | 5.82 | 5.30 | $\alpha_{MLT} = 2.0$ |
| 36 | 16.8 | 0.003 | 0.06 | 0.93 | 5.81 | 5.26 | |
| 37 | 17.2 | 0.000 | 0.00 | 0.99 | 5.83 | 5.32 | |
| 38 | 17.7 | 0.000 | 0.00 | 0.97 | 5.85 | 5.32 | |
| 39 | 18.0 | 0.000 | 0.00 | 0.99 | 5.88 | 5.39 | |
| 40 | 18.5 | 0.018 | 0.15 | 0.83 | 5.90 | 5.11 | |
| 41 | 19.4 | 0.000 | 0.00 | 0.99 | 5.91 | 5.33 | |
| 50 | 23.6 | 0.000 | 0.00 | 0.99 | 6.03 | 5.37 | |
| 60 | 26.2 | 0.000 | 0.00 | 0.14† | 6.11 | 5.47 | |
| 20 | 11.0 | 1.742 | 0.67 | 0.31 | 5.34 | 3.62 | |
| 25 | 11.1 | 0.133 | 0.42 | 0.56 | 5.55 | 4.06 | |
| 26 | 12.3 | 0.959 | 0.61 | 0.38 | 5.70 | 3.82 | |
| 27 | 12.0 | 0.059 | 0.27 | 0.72 | 5.61 | 4.75 | |
| 28 | 12.5 | 0.380 | 0.54 | 0.45 | 5.59 | 3.89 | |
| 29 | 12.9 | 0.011 | 0.20 | 0.79 | 5.66 | 5.08 | |
| 30 | 13.2 | 0.000 | 0.00 | 0.99 | 5.67 | 5.29 | |
| 31 | 13.5 | 0.000 | 0.00 | 0.97 | 5.70 | 5.32 | |
| 32 | 13.7 | 0.000 | 0.00 | 0.99 | 5.72 | 5.35 | Non-rotating Models |
| 33 | 14.6 | 0.134 | 0.36 | 0.62 | 5.76 | 4.46 | $Z = Z_\odot$; $v_{rot} = 0$ km s$^{-1}$ |
| 34 | 14.3 | 0.000 | 0.00 | 0.99 | 5.75 | 5.39 | "Dutch Wind Scheme" ($\eta = 1.0$) |
| 35 | 14.6 | 0.000 | 0.00 | 0.99 | 5.76 | 5.40 | $\alpha_{MLT} = 2.0$ |
| 36 | 14.8 | 0.000 | 0.00 | 0.99 | 5.79 | 5.41 | |
| 37 | 15.2 | 0.000 | 0.00 | 0.99 | 5.79 | 5.41 | |
| 38 | 15.6 | 0.000 | 0.00 | 0.99 | 5.81 | 5.42 | |
| 39 | 15.9 | 0.000 | 0.00 | 0.99 | 5.83 | 5.43 | |
| 40 | 16.3 | 0.000 | 0.00 | 0.97 | 5.84 | 5.43 | |
| 41 | 16.6 | 0.000 | 0.00 | 0.99†† | 5.84 | 5.40 | |
| 45 | 18.9 | 0.000 | 0.00 | 0.97†† | 5.92 | 5.40 | |
| 50 | 20.2 | 0.000 | 0.00 | 0.16†† | 5.97 | 5.47 | |
| 60 | 23.3 | 0.000 | 0.00 | 0.18†† | 6.03 | 5.39 | |
| 30 | 14.9 | 0.05 | 0.17 | 0.61 | 5.75 | 4.11 | |
| 31 | 15.1 | 0.15 | 0.42 | 0.77 | 5.76 | 4.10 | |
| 32 | 15.5 | 0.06 | 0.21 | 0.99 | 5.80 | 4.60 | |
| 33 | 16.2 | 0.00 | 0.00 | 0.99 | 5.82 | 5.40 | |
| 34 | 16.3 | 0.00 | 0.00 | 0.99 | 5.82 | 5.40 | |
| 35 | 16.6 | 0.00 | 0.00 | 0.99 | 5.84 | 5.41 | Rotating Models |
| 36 | 17.4 | 0.00 | 0.00 | 0.99 | 5.87 | 5.42 | $Z = Z_\odot$; $v_{rot} = 200$ km s$^{-1}$ |
| 37 | 17.8 | 0.00 | 0.00 | 0.99 | 5.88 | 5.42 | "Dutch Wind Scheme" ($\eta = 0.8$) |
| 38 | 17.9 | 0.00 | 0.00 | 0.99 | 5.89 | 5.43 | $\alpha_{MLT} = 2.0$ |
| 39 | 18.5 | 0.00 | 0.00 | 0.83 | 5.91 | 5.44 | |
| 40 | 20.2 | 0.01 | 0.03 | 0.15 | 5.96 | 5.10 | |
| 45 | 20.88 | 0.00 | 0.00 | 0.14 | 6.00 | 5.50 | |
| 50 | 24.58 | 0.00 | 0.00 | 0.18 | 6.05 | 5.50 | |
| 55 | 24.83 | 0.00 | 0.00 | 0.14 | 6.10 | 5.51 | |

**Note**. — † − Approximately less than 0.5$M_\odot$ of helium remains in the outer 3$M_\odot$ of this non-rotating model.
†† − Less than 0.5$M_\odot$ of helium remains in the outer 3$M_\odot$ of this non-rotating model.

**Table 6**
Remaining Hydrogen Envelope Mass for 8−20 $M_\odot$ Binary Models

| Model Name | Rotational Velocity (km s$^{-1}$) | Total Mass ($M_\odot$) | Remnant Mass ($M_\odot$) | $M_{H,1}^{env}$ ($M_\odot$) | $M_{H,2}^{env}$ ($M_\odot$) |
|---|---|---|---|---|---|
| 4M - 4M | $v_{rot} = 0$ | 8 | 7.97 | 0.00 | 1.89 |
| 5M - 5M | $v_{rot} = 0$ | 10 | 9.95 | 0.01 | 2.07 |
| 6M - 6M | $v_{rot} = 0$ | 12 | 11.91 | 0.01 | 3.04 |
| 7M - 7M | $v_{rot} = 0$ | 14 | 13.88 | 0.01 | 2.90 |
| 8M - 8M | $v_{rot} = 0$ | 16 | 15.84 | 0.01 | 3.40 |
| 9M - 9M | $v_{rot} = 0$ | 18 | 17.79 | 0.02 | 5.89 |
| 10M - 10M | $v_{rot} = 0$ | 20 | 19.74 | 0.02 | 5.67 |

**Table 7**
When the Last $0.5M_{\odot}$ is Lost to a Wind in Single Stars

| $M_{initial}$ ($M_{\odot}$) | $t_H$ ($10^6$ yrs) | $X_{surf}$ | $\log L/L_{\odot}$ | $\log T_{eff}$ (K) | Comments |
|---|---|---|---|---|---|
| 32 | 6.22 | 0.64 | 5.63 | 3.87 | |
| 36 | 5.69 | 0.06 | 5.82 | 5.31 | Non-rotating Models |
| 40 | 5.28 | 0.15 | 5.90 | 5.11 | $\eta = 0.8$ |
| 50 | 4.59 | 0.00 | 6.03 | 5.37 | |
| 60 | 4.15 | 0.00 | 6.11 | 5.47 | |
| 30 | 7.13 | 0.20 | 5.59 | 3.90 | |
| 31 | 6.92 | 0.17 | 5.61 | 3.90 | |
| 32 | 6.67 | 0.21 | 5.63 | 3.92 | |
| 33 | 6.72 | 0.04 | 5.70 | 5.14 | |
| 34 | 6.45 | 0.00 | 5.70 | 5.15 | |
| 35 | 6.29 | 0.00 | 5.72 | 5.15 | |
| 36 | 6.24 | 0.00 | 5.75 | 5.15 | Rotating Models |
| 37 | 6.07 | 0.00 | 5.76 | 5.16 | $\eta = 0.8$ |
| 38 | 5.92 | 0.03 | 5.79 | 5.13 | |
| 39 | 5.90 | 0.00 | 5.79 | 5.16 | |
| 40 | 5.77 | 0.27 | 5.82 | 4.71 | |
| 45 | 5.34 | 0.00 | 5.87 | 5.18 | |
| 50 | 4.98 | 0.00 | 5.92 | 5.17 | |
| 55 | 4.70 | 0.00 | 5.97 | 5.17 | |
| 60 | 4.49 | 0.00 | 5.17 | 5.17 | |

# The Betelgeuse Project: Constraints from Rotation

J. Craig Wheeler[1], S. Nance[1], M. Diaz[1], S. G. Smith[2], J. Hickey[1], L. Zhou[3], M. Koutoulaki[4], J. M. Fowler[5]

wheel@astro.as.utexas.edu

## ABSTRACT

In order to constrain the evolutionary state of the red supergiant Betelgeuse ($\alpha$ Orionis) we have produced a suite of ten models with ZAMS masses from 15 to 25 $M_\odot$in intervals of 1 $M_\odot$including the effects of rotation. The models were computed with the stellar evolutionary code *MESA*. For non–rotating models we find results that are similar to other work. It is somewhat difficult to find models that agree within $1\sigma$ of the observed values of R, $T_{eff}$ and L, but modestly easy within $3\sigma$ uncertainty. Incorporating the nominal observed rotational velocity, $\sim$5 km s$^{-1}$, yields significantly different, and challenging, constraints. This constraint is only matched when the models are at the base of the red supergiant branch (RSB), having crossed the Hertzsprung gap, but not yet having ascended the RSB. Models at the tip of the RSB typically rotate at only $\sim$0.1 km s$^{-1}$, independent of any reasonable choice of initial rotation. We discuss the possible uncertainties in our modeling and the observations, including the distance to Betelgeuse, the rotation velocity, and model parameters. We estimate characteristic frequencies of convective zones and propose an asteroseismological test of the models. Models at the base of the RSB may show no internal modes due to damping in the extended envelope, but models at the tip of the RSB might show characteristic times scales of order hours to a day with amplitudes of 1 – 10 millimag. We summarize various possibilities to account for the rotational velocity and suggest that one possibility is that Betelgeuse swallowed a companion star of about 1 $M_\odot$ as it ascended the RSB, in the process producing the ring structure observed at about 7' away. A past coalescence would complicate attempts to understand the evolutionary history and future of Betelgeuse.

[1]Department of Astronomy, University of Texas at Austin, Austin, TX, USA.

[2]Institute for Astronomy, University of Hawaii

[3]Department of Physics, Tsinghua University

[4]University of Crete

[5]Tufts University

*Subject headings:* stars: individual (Betelgeuse) — stars: evolution — stars: AGB and post-AGB — supernovae: general

## 1. Introduction

Betelguese ($\alpha$ Orionis) is a massive red supergiant (RSG) that is destined to explode as a Type IIP supernova and leave behind a neutron star. One of us (JCW) has long been obsessed with the uncertainty in the evolutionary state of Betelgeuse and has sought means to reduce that uncertainty. This effort, in various guises, has been informally deemed *The Betelgeuse Project.* An evolving team of undergraduates has participated in this project. Here we report on results on Betelgeuse itself, especially the constraint of its rotational state. Non–rotating models aimed at reproducing the observed aspects of Betelgeuse are given by Meynet et al. (2013) and Dolan et al. (2014). Dolan et al. found the rather surprising result that the favored mass of Betelgeuse was $\sim 19$ M$_\odot$, somewhat larger than popular estimates.

## 2. Computations

We evolved a grid of models from the Zero Age Main Sequence (ZAMS) to near the onset of core collapse using the stellar evolution code Modules for Experiments in Stellar Astrophysics (*MESA*; Paxton et al. 2011, 2013). We computed models of solar metallicity with ZAMS masses from 15 to 25 M$_\odot$ at intervals of 1 M$_\odot$ primarily using *MESA* version 6208. Most of the rotating models employed version 7624.

For one suite, the models were non–rotating and for another suite with the same ZAMS masses we assumed an initial rotation of 200 km s$^{-1}$, corresponding to about 25% of the Keplerian velocity on the ZAMS. As we will discuss below, our results do not depend sensitively on the particular choice of this initial rotational velocity; a lower value would give lower final velocities and a significantly larger initial velocity would be unphysical. Dolan et al. (2014) did a careful exploration of the sensitivity of the choice of convective and overshoot schemes. Because our principal goal was to explore the effect of rotation, we chose only the default prescriptions in *MESA*, Schwarzschild convection and an overshoot parameter of $\alpha = 0.2$. For the rotating models, we again chose *MESA* default values of mechanisms of angular momentum transport and mixing. We did not include magnetic effects (Wheeler et al. 2015). We employed the "Dutch" mass–loss prescriptions with $\eta = 0.8$. We used nuclear reaction network *approx21.* The inlist we employed is available upon request from the authors. For each ZAMS mass, the models were computed to the onset of core collapse. In practice, we

have presented some data at the beginning of core carbon burning and some at the end of core carbon burning. At those stages, there is little change in the outer, observable, characteristics. There can be significant changes in the inner convective motions that we suggest may give asteroseismological clues to the evolutionary state. In the following discussion we refer to specific models by their ZAMS mass.

## 3. Results

We compared the results of our models to the observational constraints on Betelgeuse as given by Dolan et al. (2014): $\log L/L_\odot = 5.10 \pm 0.22$; $R/R_\odot = 887 \pm 203$; $T_{eff} = 3500 \pm 200$K. Dolan et al. (2014) considered a range of possible uncertainties, including limb darkening and overshoot, but the uncertainties in $L$ and $R$ are dominated by the uncertainty in distance $D = 197 \pm 45$ pc (Harper et al. 2008), with $R \propto D$ and $L \propto D^2$. We recognize that the errors in the distance estimate are likely to be distributed asymmetrically and subject to the Lutz–Kelker–Hanson (LKH) bias that will tend to favor larger distances and hence larger radii and luminosities (Benedict et al. 2007), but for perspective, we have also examined the constraints on models considering naive $3\sigma$ errors, simply three times the $1\sigma$ errors. For $T_{eff}$, the $3\sigma$ range is $\pm 600$ K and for $R/R_\odot$, $\pm 608$. For $L$, we find $L/L_\odot = 1.3^{+0.7}_{-0.5} \times 10^5$ and $L/L_\odot = 1.3^{+2.4}_{-1.2} \times 10^5$ for the $1\sigma$ and $3\sigma$ ranges, respectively. In terms of logarithms, these values and ranges are $\log T_{eff} = 3.54^{+0.03(+0.07)}_{-0.02(-0.08)}$, $\log R/R_\odot = 2.95^{+0.09(+0.22)}_{-0.11(-0.51)}$, and $\log L/L_\odot = 5.1^{+0.19(+0.47)}_{-0.21(-0.99)}$, where the $3\sigma$ limits are given in parentheses. In addition, we have employed the constraint that the observed equatorial rotational velocity of Betelgeuse is $\sim 5$ km s$^{-1}$ (Dupree et al. 1987). The uncertainty in this quantity is itself uncertain.

In principle, the surface gravity of Betelgeuse provides another independent constraint on the ratio $R/M$. Lambert et al. (1984) adopted $\log g = 0.0 \pm 0.3$. Lobel & Dupree (2000) obtained $\log g = -0.5$ and Neilson et al. (2011) determined $R/M = 82^{+13}_{-12}(\mathrm{R}_\odot/\mathrm{M}_\odot)$. From their best–fit models, Dolan et al. (2014) obtained $R/M = 40(\mathrm{R}_\odot/\mathrm{M}_\odot)$ and $\log g = -0.05$ for their Eggleton–based code and $\log g = -0.10$ with *MESA*.

### 3.1. Non–rotating Models

Figure 1 shows representative evolutionary tracks for the 15, 20 and 25 M models, both rotating and non–rotating and the corresponding position of Betelgeuse. Figure 2 shows the interior structure of the non–rotating 20 $\mathrm{M}_\odot$ model at the point of minimum luminosity and in the stage of carbon burning.

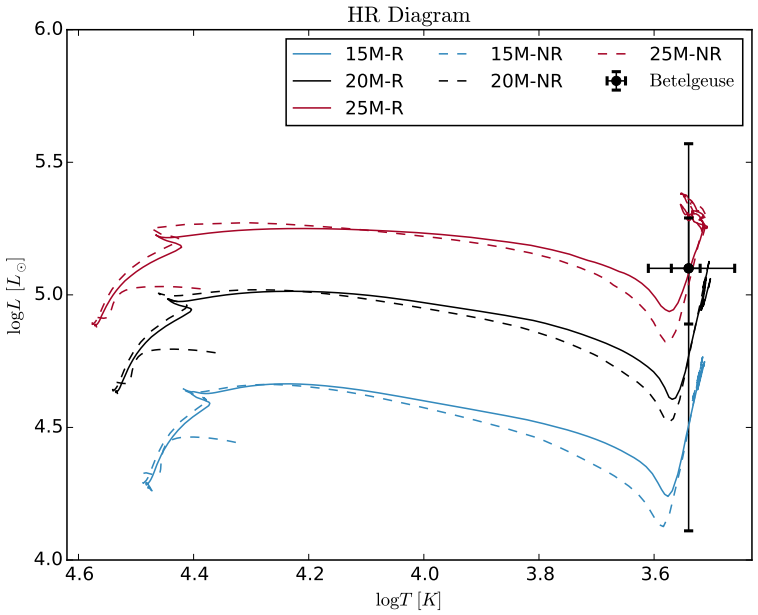


Fig. 1.— The evolutionary tracks of the models of 15, 20, and 25 $M_{\odot}$. Solid lines correspond to non–rotating models. Dashed lines correspond to models that began with an equatorial velocity of 200 km $s^{-1}$on the ZAMS. The observed position of Betelgeuse and the adopted $1\sigma$ and $3\sigma$ error bars are also shown.

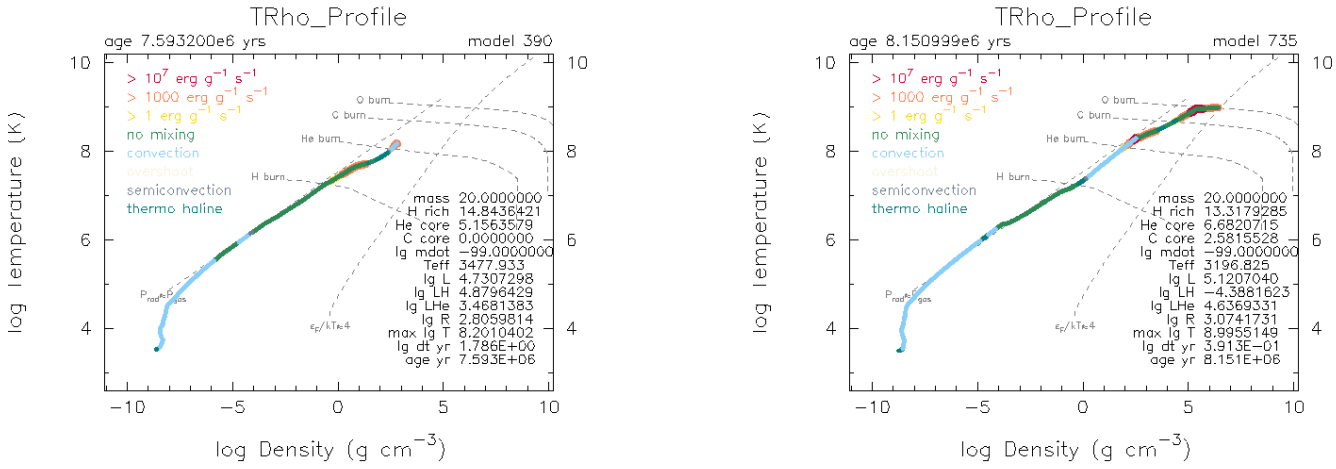


(a) (b)

Fig. 2.— Structure of the non–rotating 20 $M_{\odot}$ model in the temperature/density plane near the luminosity minimum (panel a) and near the end of the evolution (panel b).

Betelgeuse can be brought into agreement with either the minimum luminosity point at the base of the red supergiant branch (RSB) or at the tip of the RSB with a judicious choice of distance within the errors. We note that our models do not yield any blue loops, consistent with the results of Dolan et al. (2014), but that the minimum luminosity of our models is somewhat dimmer than those of Dolan et al. (2014). We find that the rotating models give somewhat brighter luminosities at the luminosity minimum at the base of the RSB in a manner consistent with the results of Meynet et al. (2013). Convective overshoot has rather little effect on the evolutionary track but can also increase the luminosity at the minimum (Dolan et al. 2014). The surface abundances of Betelgeuse are enhanced in nitrogen, depleted in carbon and display a low ratio of $^{12}C/^{13}C$, all signs that Betelgeuse has undergone the first dredge–up and hence that it must be on the ascending RSB (Dolan et al. 2014). As we shall see, this constraint is in conflict with the results of basic rotating models.

As we will show, the rotating models yield a velocity consistent with the observations near the luminosity minimum at the base of the RSB. While this constraint does not apply to the non–rotating models, we illustrate conditions near the luminosity minimum. Figure 3 (panel a) gives the distribution of $T_{eff}$ and $R$ at the point of minimum luminosity for the non–rotating models. While model 22 is in basic agreement, the models tend to be too small and hot to agree with the observations within $1\sigma$, but they mostly agree within $3\sigma$. A judicious adjustment of the distance, might then bring general agreement. Figure 3 (panel b) gives the distribution of $T_{eff}$ and $R$ at the end of core carbon burning for the non–rotating models. Models 15 to 19 match the radius to within $1\sigma$; all models agree within $3\sigma$. The temperature basically matches well, and the radius would agree with a judicious choice of distance.

Similar results pertain to the distribution of $T_{eff}$ and $L$ at the luminosity minimum as shown in Figure 3 (panel c). Model 22, 23, 24, and 25 are in basic agreement while the remaining models tend to be too dim and hot to agree with the observations within $1\sigma$. They all essentially agree within $3\sigma$. A judicious adjustment of the distance would again bring general agreement. Figure 3 (panel d) gives the distribution of $T_{eff}$ and $L$ at the end of core carbon burning for the non–rotating models. Models 17 to 23 match the luminosity to within $1\sigma$; all models agree within $3\sigma$. The temperature basically matches well, and the luminosity would agree with a judicious choice of distance.

The models that formally most closely match the observations of $T_{eff}$, $R$, and $L$ in our suite of non–rotating models is model 22 at the minimum luminosity and model 17 at the end of carbon burning.

For our 20 $M_\odot$ model, the non–rotating models give $\log g = +0.02$ at the luminosity

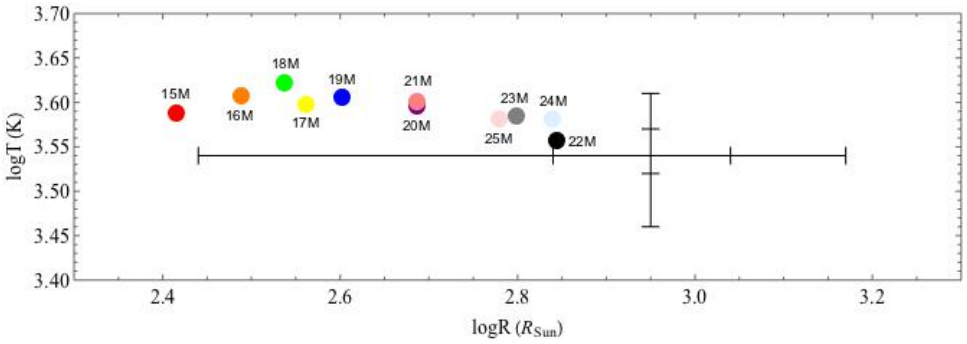


(a)

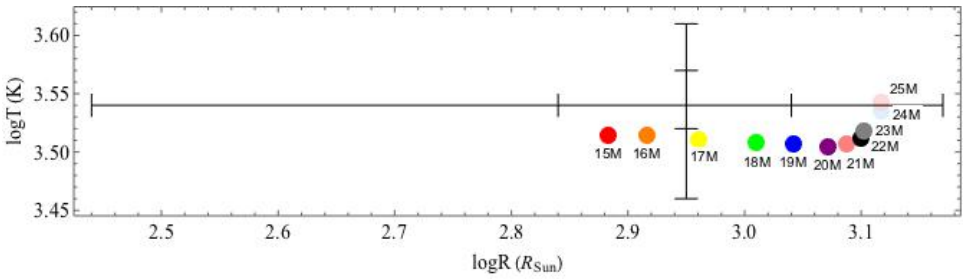


(b)

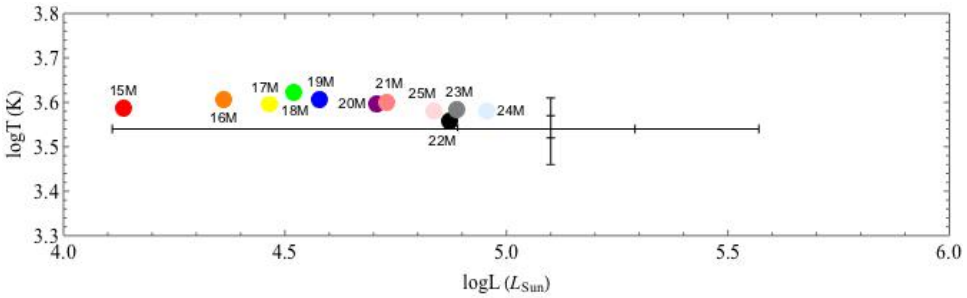


(c)

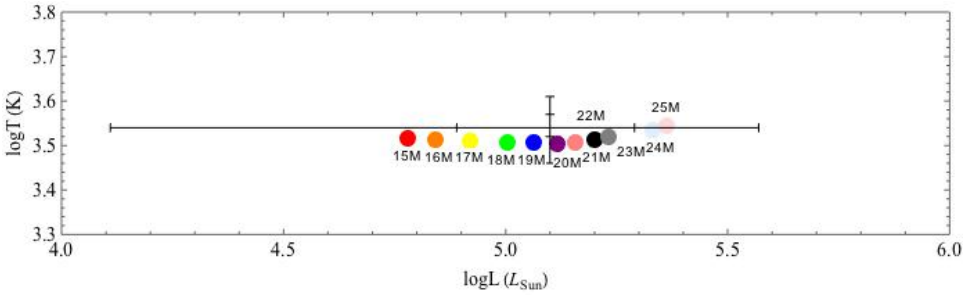


(d)

Fig. 3.— The distribution of $T_{eff}$ and $R$ is given at the base of the red supergiant branch where the luminosity is a local minimum for the non–rotating models (panel a) and at the end of carbon burning (panel b). The distribution of $T_{eff}$ and $L$ is given at the base of the red supergiant branch where the luminosity is a local minimum for the non–rotating models (panel c) and at the end of carbon burning (panel d). The point of minimum luminosity is near where the rotating models reproduce the observed rotation rate (§3.2). The observed value for Betelgeuse is given with tic marks at the $1\sigma$ and $3\sigma$ limits.

minimum and log $g = -0.3$ during carbon burning. The former is nominally too large and the latter in better agreement with the determination of Lobel & Dupree (2000), but it is difficult to rule the former out, given the level of uncertainty.

### 3.2. Rotating Models

Figure 4 gives the distribution of $T_{eff}$ and $R$ when the surface velocity is $v_{rot} \sim 5$ km s$^{-1}$ for the rotating models near the base of the RSB (panel a). Figure 4 shows that all the models are too small and dim to agree within $1\sigma$, but essentially all of them agree within the $3\sigma$ limit. Figure 4 also gives the distribution of $T_{eff}$ and $R$ at the end of core carbon burning for the rotating models (panel b). Models 15 to 20 match the radius to within $1\sigma$; all models agree within $3\sigma$. The temperature basically matches well, with the lower–mass models falling slightly low. The radius would agree for all models with a judicious choice of distance.

Similar results pertain to the distribution of $T_{eff}$ and $L$ when the surface velocity is $v_{rot} \sim 5$ km s$^{-1}$ for the rotating models near the base of the RSB as shown in Figure 4 (panel d). Model 25 agrees with the luminosity within $1\sigma$, but in temperature only at $3\sigma$. The remaining models are generally too hot and too dim, but agree within $3\sigma$. A judicious adjustment of the distance could again bring general agreement. Figure 4 also gives the distribution of $T_{eff}$ and $L$ at the end of core carbon burning for the rotating models (panel d). Models 17 to 23 match the luminosity to within $1\sigma$; all models agree within $3\sigma$. The temperature basically matches well, and the luminosity would agree with a judicious choice of distance.

The models that formally most closely match the observations of $T_{eff}$, $R$, and $L$ in our suite of rotating models are models 23 to 25 at the point where $v_{rot} \sim 5$ km s$^{-1}$ and models 16 to 20 at the end of carbon burning, ignoring the velocity constraint. These rotating models with nominally the observed rotation of Betelgeuse cannot be formally ruled out by the data. They could be accommodated if Betelgeuse were somewhat hotter than the nominal value of 3500 K and the distance were somewhat closer than the nominal 197 pc.

For our 20 M$_\odot$ model, the rotating models give log $g = +0.42$ at the luminosity minimum and log $g = -0.48$ during carbon burning. The former is substantially too large and the latter in close agreement with the determination of Lobel & Dupree (2000).

While the results for $T_{eff}$, $R$, and $L$ for the rotating models are similar to those for the non–rotating models, the rotating models yield the opportunity to examine the rotational state and compare to the observed value for Betelgeuse, $v_{rot} \sim 5$ km s$^{-1}$. Figure 5 gives the evolution of the average surface velocity for the model with ZAMS mass of 20 M$_\odot$. The

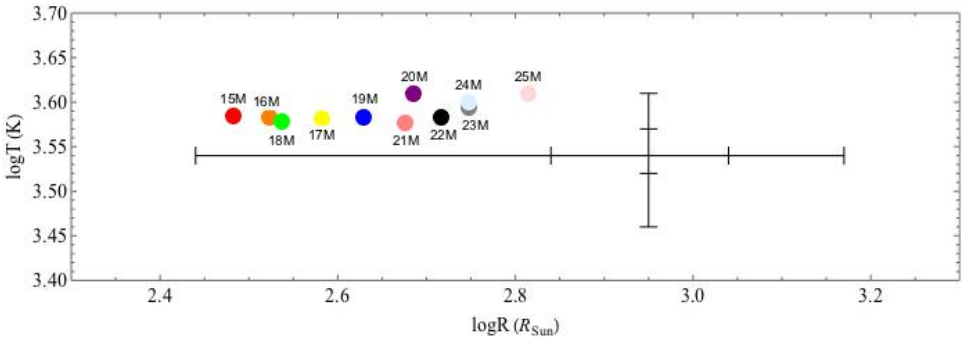


(a)

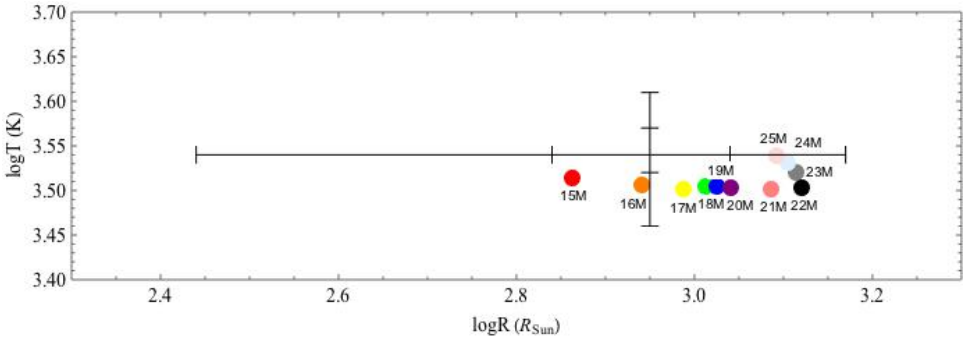


(b)

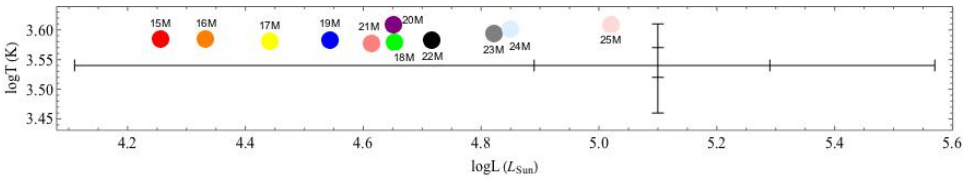


(c)

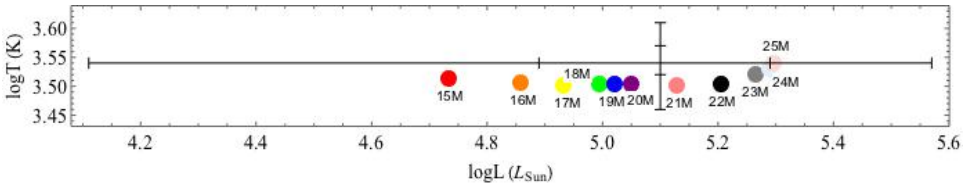


(d)

Fig. 4.— The distribution of $T_{eff}$ and $R$ is given for our rotating models at the point at the base of the red supergiant branch when the surface velocity is $\sim 5$ km s$^{-1}$ (panel a) and at the end of carbon burning (panel b). The distribution of $T_{eff}$ and $L$ is given for our rotating models at the point at the base of the red supergiant branch when the surface velocity is $\sim 5$ km s$^{-1}$ (panel c) and at the end of carbon burning (panel d). At the end of carbon burning, the surface velocity is $\sim 0.1$ km s$^{-1}$. The observed value for Betelgeuse is given with tic marks at the $1\sigma$ and $3\sigma$ limits.

models relax a little as they settle onto the ZAMS and typically begin there with a velocity somewhat greater than 200 km s$^{-1}$. The velocity has a small spike, to $v_{rot} \sim 300$ km s$^{-1}$, due to the contraction at the end of core hydrogen burning, then begins a rapid plummet as the models cross the Hertzsprung gap and proceed up the RSB. Models at the tip of the RSB that nominally reproduce the observations of Betelgeuse typically rotate at only $\sim$0.1 km s$^{-1}$, independent of any reasonable choice of initial rotation. While the uncertainty in the observed velocity is difficult to assess, this value at the tip of the RSB is far below any credible value. The rotation of Betelgeuse represents a dilemma.

Figure 4 gives the distribution of results of $R$, $T_{eff}$ and $L$ at the point where the models give a surface rotation velocity close to 5 km s$^{-1}$. These models correspond to a very peculiar, special condition. They represent the evolutionary stage after the models have crossed the Hertzsprung gap and are at essentially precisely the point of minimum luminosity before the sharp rise up the giant branch. Figure 6 gives a blow–up of the velocity evolution of of model 20 from Figure 5 and also for models 15 and 25 during the brief epochs when the models gives $v_{rot} \sim 5$ km s$^{-1}$. The velocity plunges through the observed range and on down to $v_{rot} \sim 0.1$ km s$^{-1}$ as the model rises along the RSB. The 15 M$_\odot$, 20 M$_\odot$, and 25 M$_\odot$ models pass through the interval 6 km s$^{-1}$ to 4 km s$^{-1}$ in 210, 130, and 150 y, respectively.

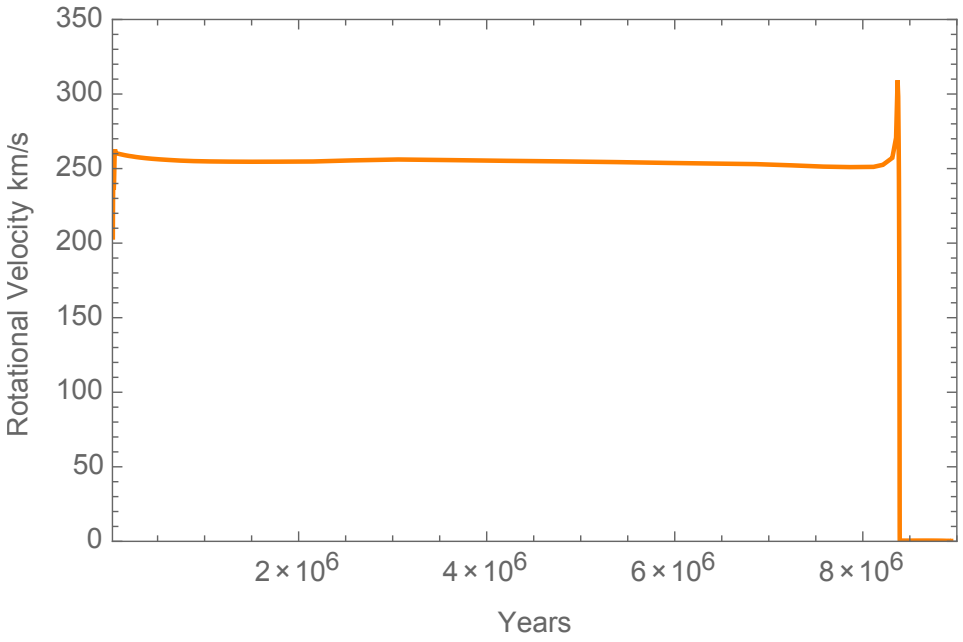


Fig. 5.— The average surface velocity as a function of time for the model of 20 M$_\odot$.

These results deepen the dilemma represented by the observed rotation of Betelgeuse. The only models that formally fit the observed data on $L$, $R$, $T_{eff}$ and $v$ are required to

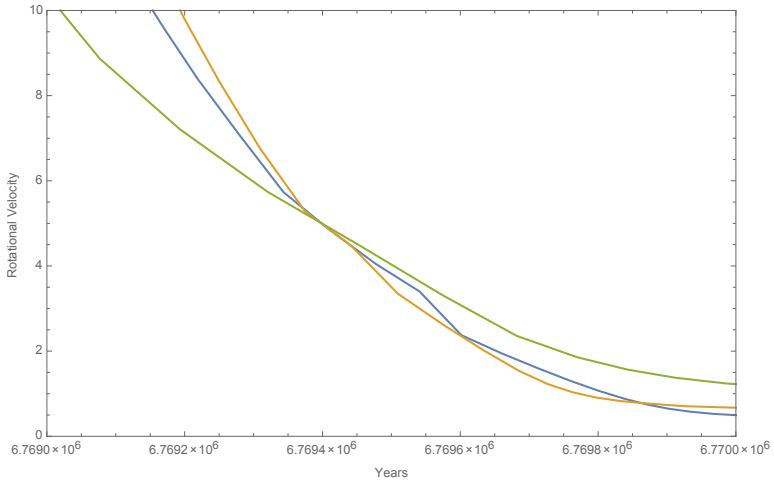


Fig. 6.— The average surface velocity as a function of time for the model of 15 $M_\odot$ (green), 20 $M_\odot$ (orange) and 25 $M_\odot$ (blue) near the base of the red supergiant branch when $v_{rot} \sim$ 5 km $s^{-1}$. The timescale given on the abscissa is for that of model 25. The other curves have been shifted in absolute time so that they align at 5 km $s^{-1}$, but the differential times with respect to the epoch of 5 km $s^{-1}$ are representative.

sit at a very special, short–lived point in the evolution. At the end of the main sequence, these stars cross the Hertzsprung gap in the hydrogen shell–burning phase. The shell tends to sit at a node at fixed radius while the helium core contracts toward helium ignition and the envelope expands. Some of the internal energy is expended in inflating the envelope and the luminosity drops as the radius expands and the temperature declines. The minimum in luminosity occurs as the envelope makes the transition from being radiative to having a deep convective structure. From that point, the star nearly reprises its proto–star phase in reverse, climbing up the Hyashi track at nearly constant temperature. For a typical model, the time to cross the Hertzsprung gap is $\sim 3 \times 10^4$ y. The time to evolve from the point of minimum luminosity and maximum post–ZAMS rotation to carbon burning is $\sim 6 \times 10^5$ y. The interval in which the models are predicted to have conditions similar to Betelgeuse and $v_{rot}$ between 1 and 10 km $s^{-1}$ is $\sim$ 1000 years. The probability that Betelgeuse happens to be in this special state of transition is low. In addition, these models give an excessively large gravity.

We also note that the hypothesis that Betelgeuse is near the point of minimum luminosity would require it to be in a stage of expanding radius. This could be inconsistent with the observation by Townes et al. (2009) that the radius of Betelgeuse systematically decreased by 15% from 1993 to 2009, about 1% per year (but see Ohnaka 2013). In the vicinity of the luminosity minimum at the base of the giant branch, our 20 $M_\odot$model increased in radius

by about 0.07% per year and our 25 $M_\odot$model increased in radius by about 0.3% per year.

### 3.3. Accounting for the Rotation

There are several possible explanations for these results. One is that we have not treated the physics of the stellar evolution properly. For instance, there may be more viscosity than computed in the default prescriptions in *MESA* that would allow a greater transport of angular momentum from the rotating core to the envelope. We have checked this aspect by computing the angular momentum in the cores of the models at the stage of carbon burning. For a typical model, 20 $M_\odot$, the angular momentum of the helium core of mass 6.2 $M_\odot$ with a surface velocity of 4.0 km $s^{-1}$ is $\approx 1.8 \times 10^{50}$ g $cm^{-2}$ $s^{-1}$ and that of the carbon core of mass 2.3 $M_\odot$ and surface velocity of 7.0 km $s^{-1}$ is $\approx 5.0 \times 10^{48}$ g $cm^{-2}$ $s^{-1}$. In carbon burning, the 20 $M_\odot$ model has a total mass of 16.6 $M_\odot$ and a hydrogen envelope of 10.4 $M_\odot$ with an outer radius of $7 \times 10^{13}$ cm. If the envelope had the same total angular momentum as the core, it would rotate at only $\approx 8 \times 10^{-4}$ the speed, or about 0.003 km $s^{-1}$, even smaller than predicted by the models. Even if all the angular momentum of the helium core core were transferred to the extended envelope, the moment of inertia of the former is too small and of the latter is too large. The envelope would still not rotate substantially faster than $\sim 0.1$ km $s^{-1}$. Massive stars are observed to rotate as rapidly as 500 km $s^{-1}$ near the ZAMS (Dufton et al. 2013), but while we have not explored these extreme initial values, it is unlikely that an increase of the initial rotation velocity by a factor of a few will lead to changes in the final envelope rotation velocity by the required factor of $\sim 50$.

Another possibility is that the observed velocity is incorrect. The velocity was determined by Dupree et al. (1987) by the use of long–slit spectroscopy to map across the (minimally) resolved surface of Betelgeuse. The result was a systematic blueshift on one limb and a redshift on the opposite of the quoted magnitude. It is at least within the bounds of credibility that the measurements were affected, perhaps even dominated, by the large–scale convective motions of the envelope for which Betelgeuse is famous.

A particularly interesting prospect is to invoke the possibility of duplicity. It is now known that a majority of O and B stars are born in binary systems (Sana et al. 2012; Dunstall et al. 2015). de Mink et al. (2014) estimate that 19% of massive, apparently single stars (those with radial velocity less than 10 km $s^{-1}$) are merged stars. Costa et al. (2015) report 17 giant stars observed with *Kepler* that show rapid rotation that might signal coalescence in a binary system.

We checked this possibility for Betelgeuse by estimating the mass of a putative com-

panion star that, having coalesced with Betelgeuse from an orbit close to the current radius, would have provided the requisite angular momentum to spin the envelope up to $v_{rot} \sim 5$ km s$^{-1}$. If we assume the companion of mass $M_2$ is a point mass and thus neglect any internal angular momentum, that the envelope of Betelgeuse was originally non–rotating, and that all the orbital angular momentum of the companion is deposited in the envelope, we can write

$$I_2\Omega_2 = I_2\frac{v_{orb}}{R_{env}} = I_{env}\Omega_{env} = I_{env}\frac{v_{rot}}{R_{env}}, \quad (1)$$

or, with $I_2 = M_2R_{env}^2$, $I_{env} \approx \frac{2}{5}M_{env}R_{env}^2$, and $v_{orb} = \sqrt{GM_{tot}/R_{env}}$,

$$M_2 \approx 0.4\ M_\odot\ M_{env,10}v_{rot,5}M_{tot,20}^{-1/2}R_{env,14}^{1/2}, \quad (2)$$

where $M_{env,10}$ is the envelope mass in units of 10 M$_\odot$, $M_{tot,20}$ is the total mass of the system in units of 20 M$_\odot$, $v_{rot,5}$ is the final rotational velocity of the envelope in units of 5 km s$^{-1}$, and $R_{env,14}$ is the radius of the primary and of the orbit of the secondary at the epoch of coalescence. This simple model suggests that the current rotation of Betelgeuse could be explained if Betelgeuse were born with a companion of mass $\sim 1$ M$_\odot$ that it swallowed as it evolved up the RSB to its current position of glory.

While this hypothesis is credible and consistent with the *a priori* estimate that Betelgeuse has a probability of $\sim 20\%$ of being born in a binary system, it raises a number of interesting issues. It is not clear that that mass and angular momentum of a companion would remain in the envelope. A companion of about a solar mass would have a mean density of about 1 g cm$^{-3}$. That density is characteristic of the base of the hydrogen envelope in the models we consider here, implying that a swallowed companion might not be dissolved until it reached the edge of the helium core. If the companion plunged down to the core, the evolution might be severely altered by anomalous burning and mixing effects. The luminosity of an evolved massive star is typically a strong function of the mass of the helium core and not the mass of the envelope. If a companion partially or totally merged with the core of Betelgeuse, then the current luminosity may be a measure of the core mass ($\sim 5$ to 6 M$_\odot$), but the mass of the envelope would be rather unconstrained and probably smaller than the estimates given here based on basic, single–star models that attempt to reproduce the luminosity, radius and effective temperature. Guessing the prior and future evolution of Betelgeuse becomes more problematic. We also note that a coalescence might have affected surface abundances, complicating their interpretation.

If there were a coalescence, there might well be some mass ejected. If a shell were ejected with a velocity near the escape velocity, $v_{esc} \sim 10v_{10}$ km s$^{-1}$ about $10^5t_5$ years ago, then if that shell expanded unimpeded it would now be at a radius, $R_{sh} = 3 \times 10^{18}v_{10}t_5$ cm. At a distance of 197 pc, the shell would have an angular radius of about 17 arc minutes. If the shell swept up matter, then this would be a rough upper limit to its location.

There is a well–observed "bow shock" about 7 arc minutes away from Betelgeuse (Noriega-Crespo et al. 1997; Decin et al. 2012). This bow shock is attributed to the wind from Betelgeuse sweeping up matter from the ISM in the direction of motion (Mohamed et al. 2012; Decin et al. 2012; Mackey et al. 2014), but it is possible that the flow of mass was impulsive rather than steady. The bow shock is rather smooth compared to numerical predictions of dynamic instabilities and is rather close to being circular (Ueta et al. 2008), again in contrast to wind simulations. It is not clear that an impulsive mass ejection at the time of companion merging would solve these issues, but this possibility (that is beyond the scope of the current paper) is worth exploring. There is also an odd, very linear feature beyond the bow shock that remains unexplained (Noriega-Crespo et al. 1997; Decin et al. 2012). The observations also show a smaller ring of material at a radius of about 4 arc minutes (Le Bertre et al. 2012). One explanation is that this is wind mass that is radiation–impeded by external radiation (Mackey et al. 2014). Such a structure could also form in the wind that was blown subsequent to the impulsive ejection we contemplate. Yet another possibility is that this inner ring is associated with the mass loss at the epoch of coalescence. This would require that the mass was ejected only about $2.4 \times 10^4$ years ago, or that there was considerable deceleration of the ejected shell.

### 3.4. Asteroseismology of Betelguse

For a judicious choice of distance, Betelgeuse might be brought into agreement with observations of $L$, $R$, and $T_{eff}$ at either the minimum–luminosity base of the giant branch or at the tip of the RSB. Single–star models give a rotational velocity of about that observed only near the minimum luminosity with the velocity at the tip of the giant branch being far below the observed value. The former seems very improbable, and this phase disagrees with the possible observed rate of contraction of the radius of Betelgeuse. The latter comports with standard assumptions, but cannot easily account for the observed rotational velocity. We need another means to determine the inner evolutionary state of Betelgeuse.

To resolve the uncertainties of the mass and evolutionary state of Betelgeuse, we need to peer inside. The most logical tool is asteroseismology (Aerts 2015). We estimated characteristic frequencies that might send acoustic signals to the surface. While it is conceivable that Betelgeuse is subject to opacity or nuclear–driven p–mode and g–mode pulsations, we made estimates guided by the notion that the inner regions of Betelgeuse will be characterized by turbulent noise associated with strong convection in the late stages of evolution as explored by Arnett & Meakin (2011), Smith & Arnett (2014), and Couch et al. (2015). We followed the techniques and methods outlined by Shiode & Quataert (2014) to determine

convective and cutoff frequencies. $MESA$ computes the distribution of convective velocities in convective regions. The distribution is not symmetric about the midpoint of typical convective zones, but nearly so. We thus estimated a characteristic timescale for the overturn of a convective eddy as

$$T_{conv} \approx \frac{2\lambda_{conv}}{v_{conv}}, \tag{3}$$

where $v_{conv}$ is the convective velocity in the middle of a convective core or shell, determined to be the half–way point in radius between boundaries of a shell or half the radius of a central convective core and $\lambda_{conv}$ is the radial extent of a convective shell or the radius of a convective core (for the core the pressure scale height might be more appropriate than the radius).

Approximating the motion of a convective eddy by a sinusoid of angular frequency $\omega_0 = 2\pi/T_{conv}$, the peak power can be written approximately as

$$P_\omega \approx \frac{sin^2[\frac{(\omega-\omega_0)T_{conv}}{2}]}{(\omega-\omega_0)^2}. \tag{4}$$

The peak power associated with this characteristic eddy overturn is thus

$$\omega \approx \omega_0 = \frac{2\pi}{T_{conv}} \tag{5}$$

with characteristic width of $\delta\omega \approx \pi/T_{conv}$[1]. We also estimated the cut–off frequency of the outer convective envelope as

$$\omega_{cut} \approx \frac{c_s}{2H_p}, \tag{6}$$

where $c_s$ is the sound speed and $H_p$ the pressure scale height in the envelope measured at 1/2 of the radius of the model. In order to propagate to the surface, $\omega_{conv} > \omega_{cut}$.

Figure 7 gives the distribution of convective frequencies and the envelope cut-off frequency as a function of ZAMS mass at the point of minimum luminosity at the base of the RSB for the non–rotating models. The outer convective envelope shows the characteristic timescale, $T \sim$ years that represents the slow overturn of the outer convective envelope. As illustrated in Figure 2, models of the type we are studying have a deeper convective shell separated from the outer envelope by a radiative region. This deeper convective region has a characteristic timescale of $T \sim$ months. Only the inner helium–burning convective core with a characteristic time of $T_{conv} \sim 10$ d might have the possibility to generate g–modes that could propagate to the surface. The frequency of this mode varies by about 20% over the range of our models, too small to be seen easily on this log plot.

[1]Note that the characteristic angular frequency in Equation 5 is a factor of $\pi$ larger than the analogous frequency defined in Shiode & Quataert (2014)

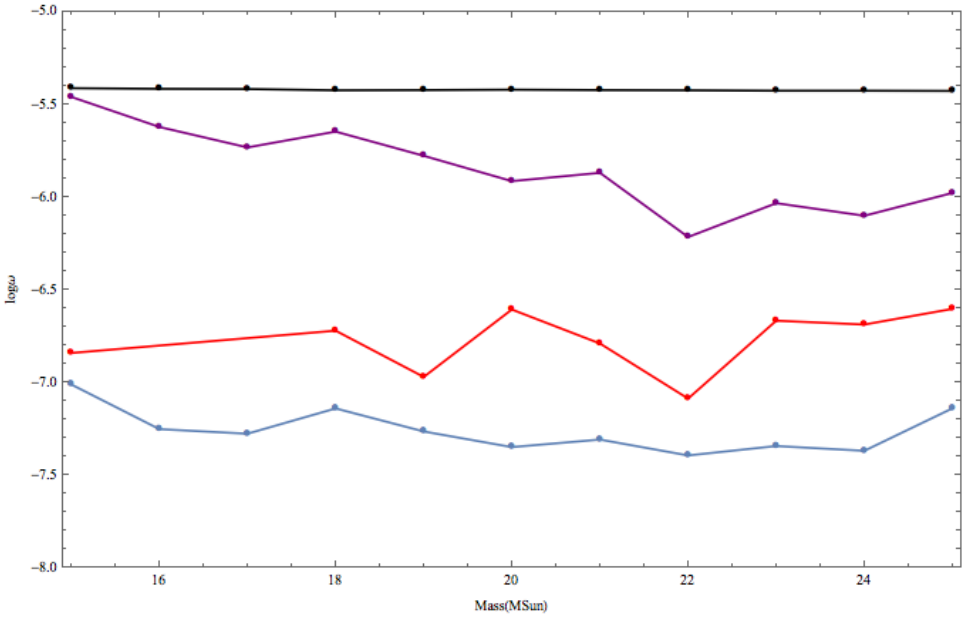


Fig. 7.— The distribution of convective frequencies and the envelope cut–off frequency as a function of ZAMS mass at the point of minimum luminosity at the base of the RSB for the non–rotating models. Similar convective structures are connected by the solid lines. The purple curve around $log\ \omega \sim -6$ denotes the cut-off frequency, below which none of the characteristic convective frequencies are expected to propagate to the surface. The blue curve around $log\ \omega \sim -7.3$ corresponds to the outer convective envelope with a characteristic period, $T_{conv}$, of years. The red curve around $log\ \omega \sim -7$ corresponds to **a separate convective** shell with a period about 3 times less. Only the convection in the helium core with a frequency $log\ \omega \sim -5.5$ denoted by the black line might be observable at the surface with an overturn time of $\sim$ 10 d.

Figure 8 gives the distribution of convective frequencies and the envelope cut–off frequency as a function of ZAMS mass at end of central carbon burning for the non–rotating models. Here the structure of the convective regions is more complex. We have attempted to identify similar regions in each mass but note that there are some models that do not display a particular structure when adjacent masses do (hence a missing "dot" in the figure) and others where a given structure is displayed by only a limited mass range. We have only attempted to capture regions of full convection and have neglected regions of semi–convection on the grounds that their slower overturn will lead to low frequencies and low power. The outer envelope again shows a period of years. The characteristic period of the convective helium shell at about 1 d and that of the separate hydrogen–rich convective shell at about 10 d (both with significant variation with mass) could, in principle, produce waves that propagate to the surface, indicating the presence of those structures. Model 19 has two convective regions with nearly the same frequency, one at $m_r = 1.30$ M$_\odot$ and one at slightly higher frequency at $m_r = 1.13$ M$_\odot$. Models 17 and 19 have an intermediate convective layer at about $m_r = 2.5$ M$_\odot$ somewhat deeper than the outer hydrogen convective shell and with somewhat higher frequency. Models 17, 18, 20, and 21 show another outer convective region with frequency close to the damping frequency that are not expected to generate an observable signal.

Figure 9 gives the distribution of convective frequencies and the envelope cut-off frequency as a function of ZAMS mass at the point near where the rotational velocity is $\sim 5$ km s$^{-1}$ at the base of the RSB for rotating models. The outer convective envelope shows the characteristic period of years. The deeper convective hydrogen shell has a characteristic period of $\sim 1$ yr. As for the non–rotating model at a similar evolutionary state, only the inner helium–burning convective core with a characteristic period of $\sim 10$ d could be expected to generate g–modes that might propagate to the surface.

Figure 10 gives the distribution of convective frequencies and the envelope cut–off frequency as a function of ZAMS mass at end of central carbon burning for the rotating models. The outer envelope shows the characteristic period of years. The characteristic period of the convective helium shell at about 0.1 to 1 d and that of the hydrogen shell at about 10 d could, in principle, produce waves that propagate to the surface. At some masses, there are intermediate convective structures with characteristic frequencies that also exceed the cut–off frequency. As for the non–rotating models, the structure near carbon burning is expected to produce a more complex spectrum with generally higher frequencies than the models near the base of the giant branch.

To estimate the possible detectability of the characteristic frequency from the convective noise, we first estimated the power associated with convective kinetic energy in each

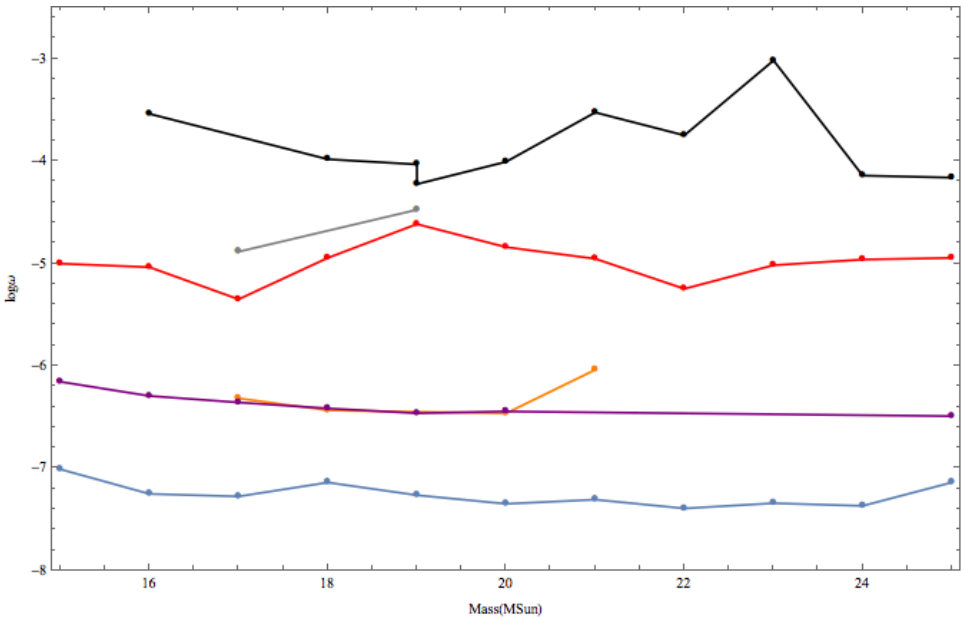


Fig. 8.— The distribution of convective frequencies and the envelope cut–off frequency as a function of ZAMS mass at central carbon burning for the non–rotating models. Similar convective structures are connected by the solid lines. The purple curve around $log\ \omega \sim -6.2$ denotes the cut-off frequency, below which characteristic convective frequencies are not expected to propagate to the surface. The blue curve around $log\ \omega \sim -7.2$ corresponds to the outer convective envelope with a characteristic period of years. The red curve around $log\ \omega \sim -5$ corresponds to a hydrogen–rich convective shell below the outer convective envelope. The black curve around $log\ \omega \sim -4$ corresponds to the helium–burning shell. Intermediate convective structures are formed at some masses. The convection in the deeper convective hydrogen and helium–burning shells might generate gravity waves that propagate to the surface with periods of about 10 d and 1d, respectively.

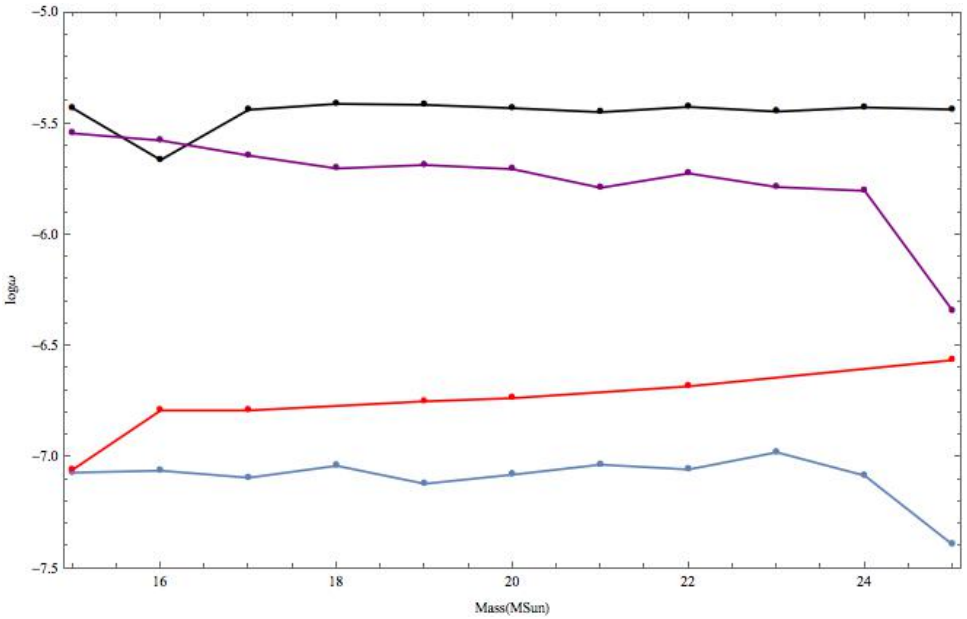


Fig. 9.— The distribution of convective frequencies and the envelope cut–off frequency as a function of ZAMS mass for the rotating models at the base of the RSB where they have rotational velocity $\sim 5$ km s$^{-1}$. Similar convective structures are connected by the solid lines. The purple curve around $log\ \omega \sim -5.3$ denotes the cut-off frequency, below which none of the characteristic convective frequencies are expected to propagate to the surface. The blue curve around $log\ \omega \sim -7.1$ corresponds to the outer convective envelope with a characteristic period of years. The red curve around $log\ \omega \sim -6.7$ corresponds to the convective hydrogen shell. Only the convection in the helium core with a frequency $log\ \omega \sim -5.4$ denoted by the black line might be observable at the surface with a period of $\sim 10$ d.

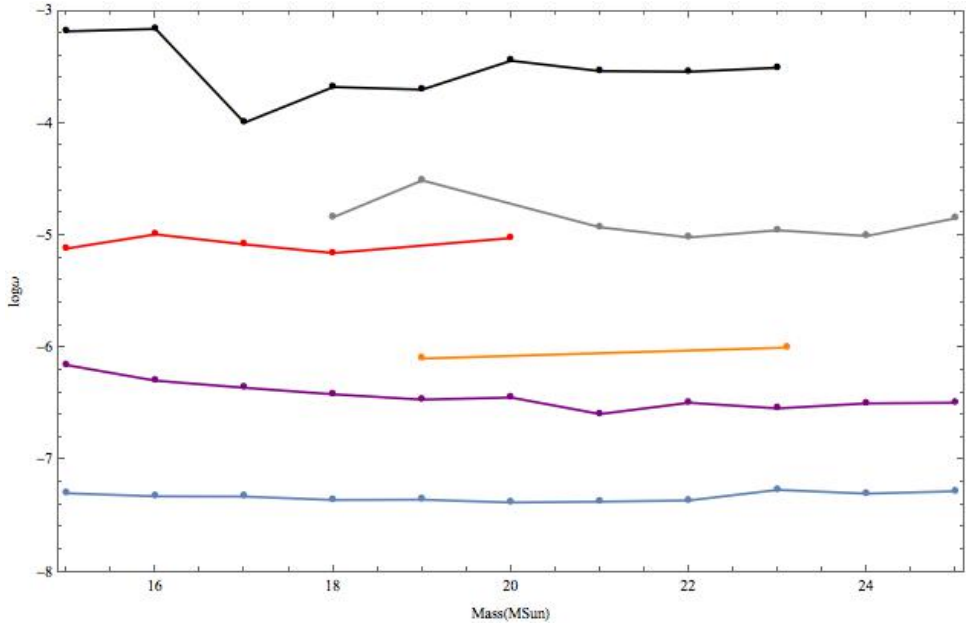


Fig. 10.— The distribution of convective frequencies and the envelope cut–off frequency as a function of ZAMS mass at central carbon burning for the rotating models. Similar convective structures are connected by the solid lines. The purple curve around $log\ \omega \sim -6.2$ denotes the cut-off frequency, below which characteristic convective frequencies are not expected to propagate to the surface. The blue curve around $log\ \omega \sim -7.2$ corresponds to the outer convective envelope with a characteristic period of years. The red curve around $log\ \omega \sim -5$ corresponds to the convective hydrogen shell. The black curve at $log\ \omega \sim -3$ to -4 corresponds to the helium–burning shell. Intermediate convective structures are formed at some masses. The convection in the convective hydrogen and helium–burning shells might generate gravity waves that propagate to the surface with periods of about 10 d and 0.1 to 1 d, respectively. The intermediate convective structures might also be observable.

convective region as

$$L_{conv} \sim \frac{1}{2}\Delta M_{conv} v_{conv}^2 T_{conv}^{-1} \sim \frac{1}{4}\Delta M_{conv} \frac{v_{conv}^3}{\lambda_{conv}} \tag{7}$$

where $\Delta M_{conv}$ is the mass in the convective region. The magnitude of the perturbation to the luminosity due to the modulation by the convective noise is

$$\delta m = | -2.5 \log \left( \frac{L_{rad} + L_{conv}}{L_{rad}} \right) | \approx 2.5 \frac{L_{conv}}{L_{rad}} \tag{8}$$

where $L_{rad}$ is the total radiated luminosity. Table 1 gives the estimated magnitude of the perturbation and the associated period, $T_{conv} = 2\pi/\omega$, for a representative sample of convective zones for models of 15, 20, and 25 $M_\odot$ in order of increasing depth in the model. Only modes with frequencies above the envelope cut–off frequency are presented.

The data in Table 1 are good to only factors of two, at best. With that perspective, the convective helium burning core might be detectable with an amplitude of tens of millimagnitudes and a characteristic period of about 10 d if Betelgeuse is near the base of the giant branch. For that evolutionary state, that should be the only detectable signal. During carbon burning, there could be a signal with a period of about 10 d, but it corresponds to the detached convective hydrogen shell beneath the outer convective envelope. In that evolutionary state, there might also be a signal with period near 0.1 d corresponding to the helium–burning shell. Taking the models at face value, the presence of that higher frequency signal might depend on the mass and the rotation state. Signals with other frequencies, as indicated in Figures 8 and 10 might also be present. The large power associated with the helium–burning shells in the rotating models at the end of carbon–burning might be an artifact of running the models somewhat longer in those cases.

The levels of perturbations given in Table 1 are, in principle, observable, but are also upper limits. There are two factors that will diminish the potential signal strength. One is the efficiency with which convective motions generate outward propagating g–mode waves. This efficiency is estimated by (Goldreich & Kumar 1990) to be of order the Mach number in the convective zone, $v_{conv}/c_s \sim 0.01$. A second factor is that the internal waves can be effervescent and subject to damping (Unno et al. 1989; Shiode & Quataert 2014). Given these factors, the helium shell may be undetectable if Betelgeuse is near the base of the giant branch. Detection of any higher–frequency modes might then directly indicate a more advanced stage of evolution, as generally expected. The question of whether any of these modes driven by internal convection are truly observable requires a deeper study than appropriate to this paper. This work may motivate such studies.

## 4. Discussion

We have used *MESA* evolutionary models to explore the mass and evolutionary state of Betelgeuse. While $T_{eff}$, $R$, and $L$ are reasonably easy to reproduce for a range of masses for judicious choices of the still rather uncertain distance, we found the observed rotational velocity difficult to reproduce. Basic rotating models yielded the observed value, $v_{rot}$ 5 km s$^{-1}$ only near the base of the giant branch. This position in the Hertzsprung–Russell diagram, while expected, could not be directly ruled out given generous estimates of the uncertainty in distance. The principal objection to this result is that the models are only in the range of the observed value of the rotation velocity for a very brief time, a few hundred years. This is as improbable as the likelihood that Betelgeuse is within a few hundred years of explosion.

We considered various factors that might mitigate our conclusion, including uncertainties in the evolutionary models, in the observations that determine the rotational velocity. We explore a solution based on the hypothesis that Betelgeuse was once a component of a binary star system and show that if it merged with a companion of about 1 M$_\odot$ when it became a red supergiant that the requisite angular momentum of the envelope might be attained. We discuss the possibility that the various shells surrounding Betelgeuse might have been associated with this merging process.

Determining the mass and evolutionary state of Betelguese requires deeper understanding. We suggest that an avenue to that understanding may lie in asteroseismology. We have made simple estimates of the power that might be generated in various convective regions that might be communicated to the surface by internal waves. The question of what convective noise frequencies might be detected at the surface of Betelgeuse is a complex one. Here we have focused on the properties of our models near the point of minimum luminosity at the end of the Hertzsprung gap when the core is well into central convective helium burning and at the end of core carbon burning; the former because that is the only place our single–star models gave the observed rotation velocity and the latter because it is representative of the late stages of the evolution of the red supergiant Betelgeuse is thought to be.

In practice, the structure of the outer convective envelope is sensitive to the precise time near the point of minimum luminosity. The extended fully–convective envelope is just forming and the models give alternate outer radiative and convective regions. By the time the models have reached the top of the giant branch, the outer, extended convective envelope is well established, but the inner structure is quite variable, with convective regions developing and effervescing. Even in the context of single-star non–rotating models, the nature of the inner convective regions, their characteristic frequencies and power and how they vary in time, require a dedicated study. Taking into account rotational mixing and the possible effects of magnetic dynamos add more complexity. If Betelgeuse has coalesced with

a former binary companion, the task, while perhaps even more important, becomes yet more complicated. An appropriate quantitative analysis might enable the determination of the current state of evolution and hence the time to explosion, the original goal.

We are grateful to E. L. (Rob) Robinson for insights, to Pawan Kumar for discussions of stellar oscillations, to Fritz Benedict for a discussion of errors in distance measurements, and to Brian Mulligan for help with Bibtex. We are especially thankful for the ample support of Bill Paxton and the MESA team. This research was supported in part by NSF Grant AST-11-9801.

## REFERENCES

Aerts, C. 2015, Astronomische Nachrichten, 336, 477

Arnett, W. D., & Meakin, C. 2011, ApJ, 733, 78

Benedict, G. F., McArthur, B. E., Feast, M. W., et al. 2007, AJ, 133, 1810

Costa, A. D., Canto Martins, B. L., Bravo, J. P., et al. 2015, ApJL, 807, L21

Couch, S. M., Chatzopoulos, E., Arnett, W. D., & Timmes, F. X. 2015, ApJL, 808, L21

de Mink, S. E., Sana, H., Langer, N., Izzard, R. G., & Schneider, F. R. N. 2014, ApJ, 782, 7

Decin, L., Cox, N. L. J., Royer, P., et al. 2012, A&A, 548, A113

Dolan, M. M., Mathews, G. J., Lam, D. D., et al. 2014, ArXiv e-prints, arXiv:1406.3143

Dufton, P. L., Langer, N., Dunstall, P. R., et al. 2013, A&A, 550, A109

Dunstall, P. R., Dufton, P. L., Sana, H., et al. 2015, A&A, 580, A93

Dupree, A. K., Baliunas, S. L., Hartmann, L., et al. 1987, ApJL, 317, L85

Goldreich, P., & Kumar, P. 1990, ApJ, 363, 694

Harper, G. M., Brown, A., & Guinan, E. F. 2008, AJ, 135, 1430

Lambert, D. L., Brown, J. A., Hinkle, K. H., & Johnson, H. R. 1984, ApJ, 284, 223

Le Bertre, T., Matthews, L. D., Gérard, E., & Libert, Y. 2012, MNRAS, 422, 3433

Lobel, A., & Dupree, A. K. 2000, ApJ, 545, 454

Mackey, J., Mohamed, S., Gvaramadze, V. V., et al. 2014, Nature, 512, 282

Meynet, G., Haemmerlé, L., Ekström, S., et al. 2013, in EAS Publications Series, Vol. 60, EAS Publications Series, ed. P. Kervella, T. Le Bertre, & G. Perrin, 17–28

Mohamed, S., Mackey, J., & Langer, N. 2012, A&A, 541, A1

Neilson, H. R., Lester, J. B., & Haubois, X. 2011, in Astronomical Society of the Pacific Conference Series, Vol. 451, 9th Pacific Rim Conference on Stellar Astrophysics, ed. S. Qain, K. Leung, L. Zhu, & S. Kwok, 117

Noriega-Crespo, A., van Buren, D., Cao, Y., & Dgani, R. 1997, AJ, 114, 837

Ohnaka, K. 2013, in EAS Publications Series, Vol. 60, EAS Publications Series, ed. P. Kervella, T. Le Bertre, & G. Perrin, 121–129

Paxton, B., Bildsten, L., Dotter, A., et al. 2011, ApJS, 192, 3

Paxton, B., Cantiello, M., Arras, P., et al. 2013, ApJS, 208, 4

Sana, H., de Mink, S. E., de Koter, A., et al. 2012, Science, 337, 444

Shiode, J. H., & Quataert, E. 2014, ApJ, 780, 96

Smith, N., & Arnett, W. D. 2014, ApJ, 785, 82

Townes, C. H., Wishnow, E. H., Hale, D. D. S., & Walp, B. 2009, ApJL, 697, L127

Ueta, T., Izumiura, H., Yamamura, I., et al. 2008, PASJ, 60, 407

Unno, W., Osaki, Y., Ando, H., Saio, H., & Shibahashi, H. 1989, Nonradial oscillations of stars

Wheeler, J. C., Kagan, D., & Chatzopoulos, E. 2015, ApJ, 799, 85

Table 1. Estimated Convective Noise Magnitude and Period

| | 15 $M_\odot$ | | 20 $M_\odot$ | | 25 $M_\odot$ | |
|---|---|---|---|---|---|---|
| | $\delta m$ (millimag) | $T_{conv}$ (days) | $\delta m$ (millimag) | $T_{conv}$ (days) | $\delta m$ (millimag) | $T_{conv}$ (days) |
| non–rotating | | | | | | |
| $L_{min}$ | | | | | | |
| He shell | 41.1 | 9.4 | 27.9 | 13 | 42.7 | 15 |
| rotating | | | | | | |
| $v_{rot} = 5$ km s$^{-1}$ | | | | | | |
| He shell | 19.8 | 10.4 | 26.9 | 13.2 | 16.8 | 16.1 |
| non–rotating | | | | | | |
| C burn | | | | | | |
| H shell | 196 | 11.2 | 648 | 10.4 | 142 | 10.6 |
| He shell | | | 206 | 0.11 | 134 | 0.14 |
| rotating | | | | | | |
| C burn | | | | | | |
| H shell | 36.6 | 12.9 | 251 | 15.4 | 634 | 11.0 |
| He shell | 16,000 | 0.11 | 10,000 | 0.10 | | |